



CHORUS

This is the accepted manuscript made available via CHORUS. The article has been published as:

Uncertainty-quantified phenomenological optical potentials for single-nucleon scattering

C. D. Pruitt, J. E. Escher, and R. Rahman

Phys. Rev. C **107**, 014602 — Published 3 January 2023

DOI: [10.1103/PhysRevC.107.014602](https://doi.org/10.1103/PhysRevC.107.014602)

Uncertainty-quantified phenomenological optical potentials for single-nucleon scattering

C. D. Pruitt,^{1,*} J. E. Escher,¹ and R. Rahman^{1,†}

¹*Lawrence Livermore National Laboratory, Livermore, CA 94550*

Optical-model potentials (OMPs) continue to play a key role in nuclear reaction calculations. However, the uncertainty of phenomenological OMPs in widespread use — inherent to any parametric model trained on data — has not been fully characterized, and its impact on downstream users of OMPs remains unclear. Here we assign well-calibrated uncertainties for two representative global OMPs, those of Koning-Delaroche and Chapel Hill '89, using Markov-Chain Monte Carlo for parameter inference. By comparing the canonical versions of these OMPs against the experimental data originally used to constrain them, we show how a lack of outlier rejection and a systematic underestimation of experimental uncertainties contributes to bias of, and overconfidence in, best-fit parameter values. Our updated, uncertainty-quantified versions of these OMPs address these issues and yield complete covariance information for potential parameters. Scattering predictions generated from our ensembles show improved performance both against the original training corpora of experimental data and against a new “test” corpus comprising many of the experimental single-nucleon scattering data collected over the last twenty years. Finally, we apply our uncertainty-quantified OMPs to two case studies of application-relevant cross sections. We conclude that, for many common applications of OMPs, including OMP uncertainty should become standard practice. To facilitate their immediate use, digital versions of our updated OMPs and related tools for forward uncertainty propagation are included as Supplemental Material.

I. INTRODUCTION

For more than fifty years, optical-model potentials (OMPs) have played an important role in nuclear scattering calculations by providing effective projectile-target interactions. Early successes in fitting basic phenomenological OMPs to elastic scattering data [1] motivated continuing theoretical improvements on several fronts, including construction of (semi-)microscopic OMPs via the local density approximation [2–5], extension to deformed and actinide systems [6, 7], and formal connection with the single-particle Green’s function via application of relevant dispersion relations [8–15]. The recent development of a global microscopic OMP [16] based on several χ EFT nucleon-nucleon (NN) potentials opens a promising new avenue for making predictions of scattering on unstable nuclides with a minimum of phenomenology. For recent reviews of OMP topics, see [17, 18].

Despite these advances, a number of basic questions remain about the uncertainty and generality of OMPs. First are questions of interpolation and extrapolation: how far can OMPs be trusted to generate reliable scattering predictions where experimental data are not available, especially away from β -stability? As new rare isotope beam facilities come online, reliable estimates of scattering on unstable targets will be needed to make sense of the wealth of new data that are anticipated. For meaningful comparison with these new data, OMP predictions should come equipped with well-calibrated uncertainty estimates, estimates that are typically absent from widely used phenomenological OMPs, such as the

Chapel-Hill 89’ OMP [19] (intended for $40 \leq A \leq 209$ from 10 to 65 MeV) and Koning-Delaroche OMP [20] (intended for $24 \leq A \leq 209$ from 0.001 to 200 MeV). In principle, a global microscopic OMP based on a χ EFT-derived NN potential, such as [16], come “naturally” equipped with uncertainties from truncation in the chiral expansion and should be less prone to under- or overfitting problems that affect phenomenological potentials. To date, however, microscopic models do not achieve the accuracy of phenomenological OMPs in regions where experimental data do exist, especially for inelastic scattering observables, which may diminish their utility for nuclear data applications. Were it available, knowledge of OMP uncertainties would help evaluators rank the relative importance of OMPs among other sources of uncertainty that enter reaction models, such as nuclear level densities and γ -ray strength functions [21].

The second type of questions concern the functional form of potentials and their capacity to realistically describe the underlying physics. As a simple example, the Koning-Delaroche OMP includes an imaginary spin-orbit term, but the Chapel Hill ’89 OMP does not. Does inclusion of this term result in meaningful differences in scattering predictions, and if so, which experimental data actually constrain its parameters? The form of nonlocal terms [22–24], shape of the hole potential and relation to dispersive correctness [13], and the correct dependence of parameters on nuclear asymmetry [25] are important open topics that would benefit from a firmer understanding of uncertainty in extant OMPs.

To clarify these issues, several recent studies have investigated uncertainty-quantification (UQ) techniques for phenomenological OMPs, including direct comparisons of frequentist and Bayesian methods for model calibration [26, 27], introduction of Gaussian process priors for energy-dependent parameters [28], and introduction

*Corresponding author: pruit9@llnl.gov

†Present address: University of Tennessee, Knoxville, TN 37996

of an ad-hoc dedicated “model uncertainty” term in a dispersive OMP analysis [29]. The ambitious study of [21] confronts the mature reaction code TALYS [30] with virtually the entire EXFOR experimental reaction database [31] with the specific intent of generating uncertainties for evaluations. Such theoretical studies are being complemented by the creation of templates for experimentalists for capturing the many (often undercharacterized) sources of uncertainty in experimental measurement [32–34], designed specifically so that newly collected data will be maximally useful for theory and evaluation efforts going forward. Most recently, the work of [28] proposes a statistically sound, reproducible pipeline for nuclear data evaluations, including characterization of OMP uncertainties, demonstrating the potential to accelerate and standardize the challenging process of evaluation.

Despite these methodological improvements over the last decade, many OMP users do not yet consider the OMP contribution to the uncertainty budget of their applications, either because it is assumed to be negligible or because tools to do so are difficult to use. Those that do (e.g. [35, 36]) typically estimate uncertainty qualitatively by manually varying a handful of parameters thought to be important and by comparing predictions from a handful non-UQ OMPs against each other by eye. Even when OMP parameter uncertainty estimates are available (e.g., [30]), they are more often based on hard-earned evaluator intuition rather than on detailed tests of empirical performance. In the ideal case, each OMP would ship with complete covariance information for potential parameters, be tested against trusted, easily-accessed data libraries, be based on reproducible statistical practices and stated assumptions, and make it easy for any downstream user to forward-propagate OMP uncertainty into their research application. Robust OMP UQ of this type would be a building block for larger UQ efforts such as the evaluation efforts mentioned earlier [21, 28] or improved experimental analysis pipelines. Motivating and demonstrating such a framework for phenomenological OMP UQ is the main goal of the present work.

To demonstrate our approach, we apply it to both the Koning-Delaroche global OMP (KD) [20] and the Chapel-Hill ’89 OMP (CH89) [19], yielding two new uncertainty-quantified OMP ensembles we designate KDUQ and CHUQ, respectively. To train these OMPs, we recompiled the same training data corpora as used in the original treatments (we refer to our recom compilations as the CHUQ corpus and KDUQ corpus). The resulting UQ OMPs can be directly inserted into existing user codes to incorporate the parametric uncertainty of these OMPs. By applying our approach to multiple OMPs and comparing with microscopic and semi-microscopic alternatives, we can develop insight into how the next generation of uncertainty-equipped potentials can be gainfully constructed. In particular, we will emphasize the importance of two key steps in fitting phenomenological OMPs — managing *outliers* and *experimental uncertainty underestimation* — that are paramount for empirical UQ, both in OMPs and otherwise.

Our findings are organized in the following sections. Section II introduces the generic parameter inference problem and its application to OMP fitting, including challenges faced in the original CH89 and KD analyses. Section III proposes a new likelihood function and inference strategy based on Markov-Chain Monte Carlo (MCMC) that we argue is better suited for generating realistic OMP uncertainties. Section IV applies this strategy to retrain the KD and CH89 OMP forms against their original training data, yielding updated, uncertainty-quantified OMPs: KDUQ and CHUQ. Section V illustrates the impact of KDUQ and CHUQ both on Hauser-Feshbach calculations for two radiative capture test cases and on the reliability of OMP extrapolation along neutron-proton asymmetry. Section VI summarizes our findings. Following the main text, further technical details appear in the Appendix and three sections of Supplemental Material [37], including explicit definitions of the OMPs and scattering formulae, all experimental data used for training and testing, and our recommended KDUQ and CHUQ parameter values for future use. We hope that by providing thorough documentation, readers will be able to reproduce or extend our results without guesswork.

II. CHALLENGES IN OMP PARAMETER INFERENCE

In this section, we first present a generic parameter inference problem, illustrating some common challenges with a pedagogical example. We then turn to the original KD and CH89 analyses, showing that certain assumptions, while necessary for making these canonical analyses tractable, can result in overconfidence in the fitted parameters.

A. Generic parameter inference

The goal of a parameter inference problem is to determine optimal parameters for a given functional form, where “optimal” usually means best matching a corpus of training data. In the specific case of OMP optimization, the OMP constitutes a model M with unknown, possibly correlated potential parameters θ , and the task is to determine an optimal set of parameters θ_{opt} that minimizes the residuals between experimental scattering data and scattering-code predictions made using M . (In these and all following definitions, we use bold typeface to denote a vector or matrix quantity.) A natural starting point for the probability density function of θ is to use a k -dimensional normal distribution:

$$p(\theta) = \frac{1}{\sqrt{(2\pi)^k |\Sigma|}} e^{-\frac{1}{2} \mathbf{r}^\top \Sigma^{-1} \mathbf{r}} \quad (1)$$

$$\mathbf{r} = \theta - \theta_{opt}.$$

Here, Σ is the $k \times k$ covariance matrix associated with

θ . If θ_{opt} and Σ were known, the inference problem would be solved (at least up to the assumption of multivariate normality), with Σ holding the variance information enabling downstream uncertainty propagation. Because we do not have direct measurements of θ , only experimental scattering measurements, we cannot use Eq. 1 directly to train the model. Instead, we need to construct a likelihood function that connects the probability of observing a given experimental value given a candidate parameter vector. For OMP optimization, this involves mapping a candidate θ to predicted scattering observables via a scattering code, evaluated at the relevant experimental indices (e.g, scattering energy, angle, target). This mapping is highly nonlinear in θ as it involves, among other things, solving for the scattering matrix. Because the covariance matrix between experimental measurements is rarely known (discussed in detail in [21]), connecting OMP parameters with experimental data via selection of a likelihood function requires making certain assumptions about the scattering data. The overwhelming majority of past OMP analyses (including CH89 and KD) use a maximum likelihood approach based on some version of weighted-least-squares for their likelihood function:

$$L(\mathbf{y}|\mathbf{x}, \delta_{\mathbf{y}}, \theta) = e^{-\frac{1}{2} \sum_i \frac{r_i^2}{\delta_{y_i}^2}} \quad (2)$$

$$r_i = y_i - M(\theta, x_i).$$

In this expression, for the i^{th} training data point, x_i are the experimental conditions (such as energy, angle, etc.), y_i is the observed value, such as the cross section, and δ_{y_i} is the reported uncertainty of the observed value. Thus $(\mathbf{x}, \mathbf{y}, \delta_{\mathbf{y}})$ denotes the entire training corpus. Experimental data also often include an estimate of uncertainty in the experimental conditions $\delta_{\mathbf{x}}$ but these are usually omitted from the OMP analysis as they are more difficult to incorporate using standard optimization approaches. The predicted values, $M(\theta, \mathbf{x})$, are an output of the scattering code evaluated at each \mathbf{x} and using the OMP realization $M(\theta)$ for the projectile-target interaction.

If several conditions apply, including model linearity in the parameters, experimental uncertainties characterized by a known, positive-definite covariance matrix, and measurement samples being drawn from the same underlying distribution, the weighted least-squares estimator (Eq. 2) guarantees an analytic solution that minimizes bias in θ_{opt} [38]. Unfortunately for OMP analysts, each of these conditions is violated in traditional OMP optimization analyses that are concerned primarily with θ , and these violations are especially problematic for the present UQ task (Σ estimation). Most impactful is the weighted-least-squares assumption that experimentally reported uncertainties are independent and complete (that is, that the vector of individual data point uncertainties $\delta_{\mathbf{y}}$ fully represents the true, unknown data covariance matrix). In effect, this assumption assigns more independent information to residuals than they ac-

tually have, making the inference problem erroneously overdetermined and causing bias in θ_{opt} and underestimation of θ_{opt} uncertainty. Even if the full experimental data covariance were known, the OMP, by definition, is a projection of the true projectile-target interaction onto a reduced space of simple potential forms. As such we should expect it to suffer at least somewhat from “model defects” that, if unaccounted for during inference, may lead to overconfidence in an incorrect θ_{opt} , as demonstrated for a simple physical model in [39]. Further, model nonlinearity in θ means that the likelihood function surface is not guaranteed to be convex, which can stymie simple optimization approaches such as gradient descent but which may be tractable with other optimization algorithms such as, e.g., simulated annealing.

B. A toy model

To illustrate how outliers and uncertainty underestimation impact parameter inference, we present a toy problem using a simple linear model. Imagine we wish to describe some generic phenomenon, $T(x)$, that occurs on a domain $x \in [-1, 1]$. The true $T(x)$ is:

$$T(x) = 2.5P_0(x) + 2.0P_1(x) + 1.5P_2(x) + 1.0P_3(x), \quad (3)$$

where P_n is the n^{th} Legendre polynomial. Suppose we know the functional form of $T(x)$ but not the values of the coefficients, which we would like to learn through inference against data. So we collect i observations \mathbf{y} at experimental conditions \mathbf{x} , using a device subject to measurement uncertainty. Aware of this uncertainty, we estimate measurement imprecision for each data point as $\delta_{\mathbf{y}}$. We then define a model, M , and compare model predictions $M(\mathbf{x}, \theta)$ to the measured data, where θ are the n unknown coefficients that we want to learn. Because our model is linear in θ and our data measurements are independent and uncorrelated, Eq. 2 provides the best unbiased estimator of the true coefficients, denoted θ_{true} . We can find an optimum set of parameter values θ_{opt} analytically using maximum likelihood estimation or numerically using, e.g., gradient descent until we reach some threshold for convergence. The covariance matrix at θ_{opt} is the inverse of the Hessian matrix $\mathcal{H}(\theta_{opt})$, which can be easily assessed numerically.

So far, we have described a simple, generic inference problem and its solution. We now consider four possible scenarios for solving this problem, each involving a different possible distribution for \mathbf{y} and $\delta_{\mathbf{y}}$. These differing distributions are plotted in panels (a) to (d) of Fig. 1, and defined according to:

$$y_i \sim \mathcal{N}(T(x_i), 0.32^2)$$

$$\delta_{y_i} = 0.32T(x_i) \quad (4)$$

$$y_i \sim \mathcal{N}(T(x_i), 0.32^2)$$

$$\delta_{y_i} = 0.10T(x_i) \quad (5)$$

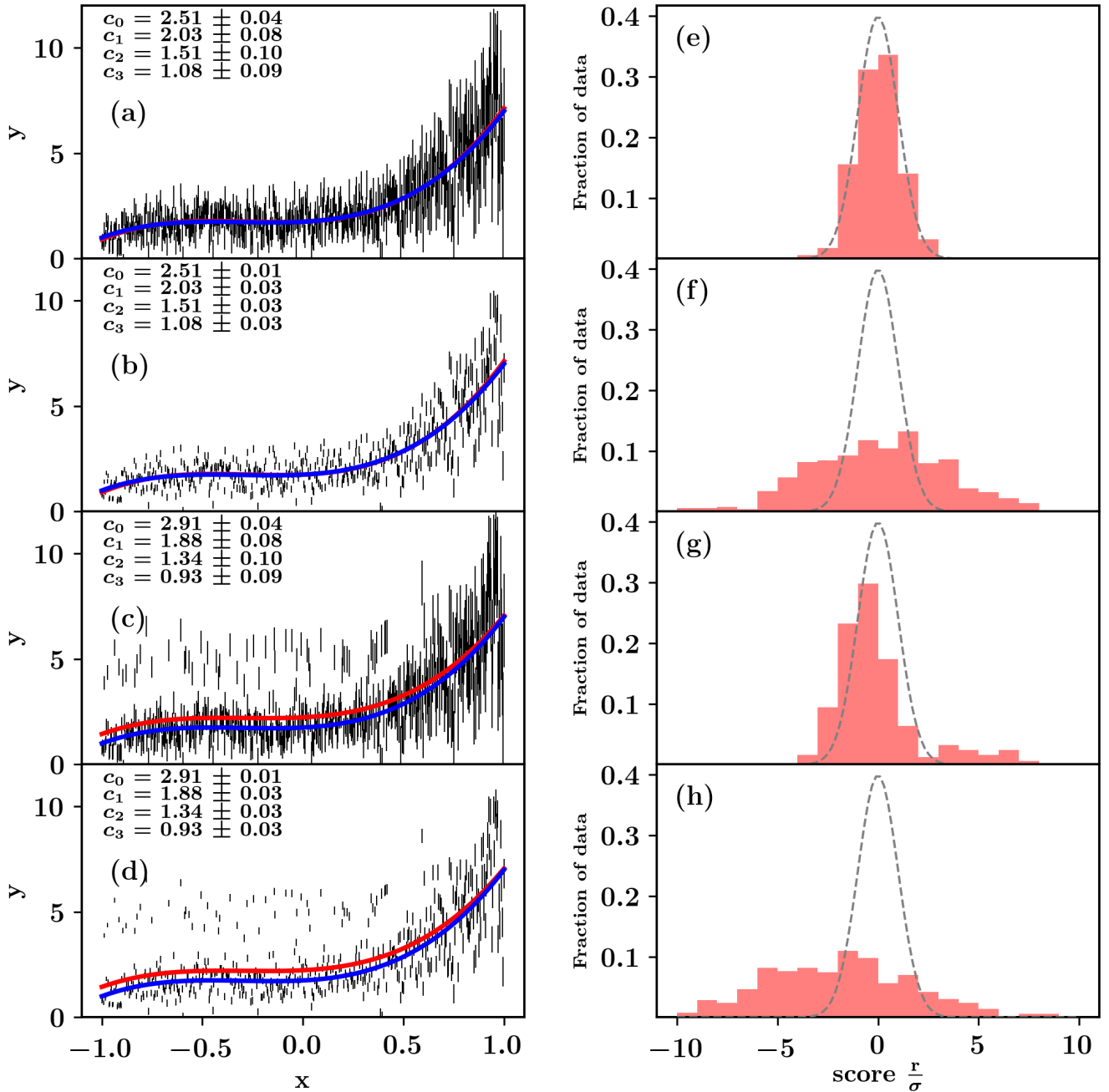


FIG. 1: The four data-fitting scenarios for the toy model discussed in the text are compared. Panel (a) shows a fit to data with accurate uncertainty estimates and no outliers. Panel (b) shows a fit to data with underestimated uncertainties and no outliers. Panel (c) shows a fit to data with accurate uncertainty estimates but with outliers. Panel (d) shows a fit using data with both underestimated uncertainties and with outliers. The simulated data used for fitting are shown as black bars, the “true” underlying function used to generate the data is shown as a blue line, and the fit to the “experimental” data is shown in red. In panels (e) to (h), the normalized residuals for data in the corresponding plots are histogrammed. A normal distribution with $\mu = 0$ and $\sigma^2 = 1$ (gray dashed line) is shown for reference.

$$\begin{aligned} y_i &\sim \mathcal{N}(T(x_i), 0.32^2) + \alpha \\ \delta_{y_i} &= 0.32T(x_i) \end{aligned} \quad (6) \quad \text{for each } i, \text{ where}$$

$$\begin{aligned} y_i &\sim \mathcal{N}(T(x_i), 0.32^2) + \alpha \\ \delta_{y_i} &= 0.10T(x_i), \end{aligned} \quad (7)$$

$$\alpha \begin{cases} \sim \mathcal{N}(3, 0.6^2), & 10\% \text{ probability,} \\ = 0, & 90\% \text{ probability.} \end{cases}$$

In this notation, $\sim \mathcal{N}(\mu, \sigma^2)$ refers to sampling from a

normal distribution of mean μ and variance σ^2 .

We begin with the first scenario, shown in panel (a) of 1. This is the best-case scenario, given the assumptions appropriate for weighted-least-squares: our measuring device suffers from zero bias and the true mean measurement uncertainties $\delta_{\mathbf{y}}$ are known (Eq. 4). For example, our measuring device exhibits independent statistical and systematic uncertainties of 10% and 30%, yielding a total 32% total uncertainty via addition in quadrature. Because both the measured data and their uncertainties are faithful to the true underlying distribution, our estimated θ_{opt} match θ_{true} , up to the estimated uncertainty of θ_{opt} . Panel (e) shows that the distribution of standardized residuals between our model’s predictions and the corresponding experimental data are distributed according to a normal distribution with unit variance.

Panel (b) of Fig. 1 shows the outcome of the second scenario: our measuring device performs identically as in the first scenario, but now our estimates of $\delta_{\mathbf{y}}$ are too small (Eq. 5). This could arise if, for instance, both statistical and systematic uncertainty contribute to the overall uncertainty of our measuring device, but we have only recognized and reported the statistical uncertainty. Because the minimum of our weighted-least-squares likelihood function is not affected by overall rescalings of $\delta_{\mathbf{y}}$, we recover the same θ_{opt} as in the first scenario. However, our *uncertainty* estimates of θ_{opt} have shrunk by a factor of three — the same factor by which we underestimated the measurement uncertainty — because the Hessian $\mathcal{H}(\theta_{opt})$ scales proportionally with $\delta_{\mathbf{y}}$. Panel (f) shows that while the standardized residuals remain normally distributed with a mean of zero, they are more dispersed than the reference distribution. Thus, underestimation of experimental uncertainties directly causes underestimation of parametric uncertainties. This is a generic feature of parameter inference and, as we will show in the following section, affects most previous OMP analyses.

Panel (c) of Fig. 1 presents a third scenario: as in the first scenario, we have accurately estimated the experimental uncertainty δ , but now our experimental device occasionally returns anomalous measurements (so-called “outliers”). The simulated data \mathbf{y} have been drawn according to 6: each measurement has a 10% chance of being shifted upward by α , which is an artificial “outlier factor”. This is meant to represent a more realistic situation in which some fraction of experimental data are inconsistent with the model, either because of model defects or because of problems during experimental data collection. The outliers “pull” on the likelihood function, causing our recovered θ_{opt} to differ from those of the previous scenarios, but, because our $\delta_{\mathbf{y}}$ are the same as in the first scenario, our *uncertainty* estimates of θ_{opt} do not change. The parameter bias appears in panel (g) as asymmetry in the standardized residuals with respect to the reference distribution, even as the variance of the residuals is the same as in the first scenario. We note that even if our measuring device returned no outliers, if our underlying model was incorrect (i.e., model defect),

certain data would appear to be outliers, and we would obtain a similar result.

Finally, panel (d) of Fig. 1 combines the second and third scenarios: \mathbf{y} contains occasional outliers and $\delta_{\mathbf{y}}$ are overconfident (Eq. 7). Accordingly, our estimated θ_{opt} is biased and our uncertainty estimates of θ_{opt} are overconfident about the biased estimates. Both the bias and the dispersion of the normalized residuals are visible in panel (h). This scenario is the best analog to the OMP optimization task. For us to obtain well-calibrated uncertainties that span the experimental data, our loss function and optimization strategy must address both challenges: namely, underestimation of experimental (co)variances, and fundamental discrepancies between the model and data either due to model defects or problems with experimental data collection (which we do not attempt to disentangle).

C. Challenges for CH89 and KD

The difficulties of using weighted-least-squares estimators are well-known to OMP designers, including those of CH89 and KD. A common symptom is that initial fits to experimental data are often grossly unsatisfactory, clearly missing “the physics” present in the scattering data, leading to manual parameter adjustment. The authors of CH89 comment that, early in their analysis, there were often “significant contributions from the data that the model is not able to describe” even when training to a single scattering data set. They tested several alternative loss functions but found that in “reduc[ing] the emphasis of outlying points” they “lost sensitivity to even the good data”. After testing various functions, their compromise was to introduce a weight factor to their likelihood function for each data set s , equal to the minimum loss for that data set obtained in a fit to *only* that data set, i.e.,

$$L(\mathbf{y}|\mathbf{x}, \delta_{\mathbf{y}}, \theta) = \sum_s \frac{L_s(\theta|\mathbf{x}_s, \mathbf{y}_s)}{\min(L_s^{loc}(\theta|\mathbf{x}_s, \mathbf{y}_s))}, \quad (8)$$

where L_s is the contribution from data set s to the overall weighted-least-squares fit as in Eq. 2. By deemphasizing data sets that were poor matches to the form of their OMP, they achieved a better visual fit to their training data. However, this solution also introduces problems: the introduced weights are not easily interpreted nor do they preserve the normalization of the likelihood function, which is important for estimating Σ . However, because finding θ_{opt} is insensitive to overall rescalings of L , most past authors have been willing to sacrifice the possibility of accurately estimating Σ in order to improve their single “best-fit” parameter vector.

Koning and Delaroche identified this issue in their global OMP characterization as well and also provided extensive quantitative evidence that traditional OMPs are incapable of reproducing the bulk of experimental data within the range of reported experimental uncertainties. In Table 12 of their OMP analysis [20], they

present sums of uncertainty-weighted square residuals per degree of freedom (a reduced- χ^2 metric) for several prominent OMPs against a variety of experimental data sets. In their analysis, a value near unity was taken as an indication of good model-data agreement. For the widely used global OMPs they considered, they found values of χ^2/N ranging from 6.3 to 11.2 for differential elastic scattering cross sections and from 2.3 to 9.2 for neutron total cross sections. Using their new potential (KD), they found values of χ^2/N ranging from 4.5 to 7.4 for differential elastic scattering cross sections and from 1.2 to 6.7 for neutron total cross sections, depending on the experimental data corpus tested against. They echoed the comments of the CH89 authors, noting that “the optimization procedure is very sensitive” to underestimations in reported experimental uncertainties such that “even a slightly incorrect error estimation can easily vitiate an automated fitting procedure”. In [21], Koning further analyzed model-experiment discrepancies across the EXFOR database and combined several proposed remedies into an “evaluated” χ^2 expression meant to overcome the issues of using naïve weighted least squares.

To better understand these discrepancies between the trained model and training data, we began by reproducing the original CH89 and KD analyses. Figure 2 summarizes the performance of the standard CH89 and KD potentials against the experimental data used to train them, as reconstructed in the present work. For each experimental datum, the normalized residual for that datum (r/δ_y) was tabulated, then all residuals histogrammed according to data type. In addition, in panel (b), two dotted curves show the performance of CH89 when the CH89 parameters are resampled according to the parameter covariance matrix presented in the original publication. If the assumptions underpinning weighed-least-squares were fulfilled, each line should follow the gray dashed line (a normal distribution with unit variance), indicating that the CH89 and KD predictions match the mean of the experimental data used to train them, and that the training data are dispersed about the predictions in keeping with their reported uncertainties. In reality, all types of scattering data show a variance several times larger than unity, an indication either of underestimation of experimentally reported uncertainties or of significant model deficiencies, or both. The means of the distributions are offset to varying degree, indicating that the canonical θ_{opt} for these OMPs retain some bias with respect to the underlying experimental data. Table I lists the mean, standard deviation, and skewness of these observed distributions for each data type used to train the CH89 and KD OMPs. This confirms the issues identified by past authors: clearly, these OMPs do not span the variance of their training data, and for some data types, predictions show systematic bias with respect to experiment.

The comparison of these canonical OMPs with their training data led us to investigate the self-consistency of the training data themselves. We discovered that these training data sets were often inconsistent, in the sense

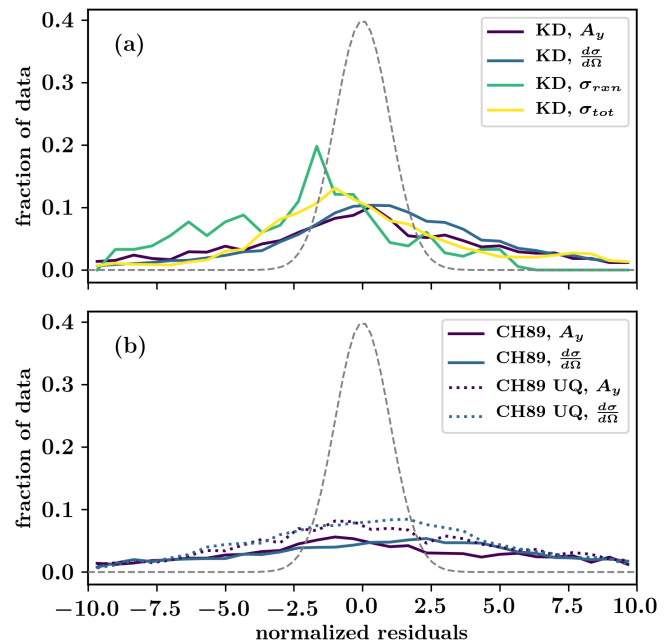


FIG. 2: The distribution of normalized residuals (r/δ_y) between the original KD and CH89 OMPs and their training data, as reconstructed in this work. KD is shown in panel (a) and CH89 in panel (b). Residuals are histogrammed by data type, with all available proton and neutron data for that data type included (in contrast with Table I which discriminates by projectile). In panel (b), CH89 UQ refers to a version of the CH89 OMP that includes the parametric uncertainties reported in the original work, which we have sampled here as $\theta \sim \mathcal{N}(\theta_{CH89}, \Sigma_{CH89})$, with θ_{CH89} being the canonical CH89 “best fit” parameter vector, and Σ_{CH89} being the canonical CH89 covariance matrix published in the original treatment.

that *no* plausible model could simultaneously fit them. This implies that for data routinely used in OMP training, the reported experimental uncertainties may be significantly underestimated. Figure 3 illustrates the problem: in panel (a), five independent, representative elastic scattering data sets for neutrons on ^{40}Ca at 14 ± 0.1 MeV from the EXFOR database [31] are shown. Each is comparable to the elastic scattering data sets used to train the KD and CH89 OMPs. To facilitate comparison between these data sets, which were measured at different angles, we describe their mean behavior as:

$$f(\theta) = \sum_{n=0}^{10} c_n p_n(\theta) \quad (9)$$

where $p_n(x)$ are Legendre polynomials. A simple weighted-least-squares fit was performed to optimize the polynomial coefficients c_n . When the fit and training data are compared, the normalized residuals are inconsistent with one another at the several- σ level, as shown in panel (b) of the same figure, due to underestimation of experimental uncertainties. Considering that these data were all collected for the same projectile-target sys-

TABLE I: Mean (μ_1), standard deviation (μ_2), and skewness (μ_3) for the distribution of standardized residuals between the original KD and CH89 OMPs and their training data, as reconstructed in this work. Results are tabulated separately for protons and neutrons. The columns labeled CH89 UQ refer to a version of the CH89 OMP that includes the parametric uncertainties reported in the original work, which we have sampled here as $\theta \sim \mathcal{N}(\theta_{CH89}, \Sigma_{CH89})$, with θ_{CH89} being the canonical CH89 “best fit” parameter vector, and Σ_{CH89} being the canonical CH89 covariance matrix estimate published in the original treatment.

Proton data							
	CH89		CH89 UQ		KD		
	$\frac{d\sigma}{d\Omega}$	A_y	$\frac{d\sigma}{d\Omega}$	A_y	$\frac{d\sigma}{d\Omega}$	A_y	σ_{rxn}
μ_1	0.5	-3.2	1.1	0.7	0.7	-0.4	-2.4
μ_2	29.8	30.7	9.6	7.0	18.6	18.4	3.7
μ_3	-2.1	-3.2	-1.6	0.6	-1.0	-3.3	-1.0

Neutron data							
	CH89		CH89 UQ		KD		
	$\frac{d\sigma}{d\Omega}$	A_y	$\frac{d\sigma}{d\Omega}$	A_y	$\frac{d\sigma}{d\Omega}$	A_y	σ_{tot}
μ_1	-1.9	1.4	-1.7	1.2	-2.1	0.8	-0.3
μ_2	5.0	6.5	4.0	4.4	4.8	6.8	25.2
μ_3	-0.7	0.5	-0.8	0.3	-0.7	-19.9	-17.5

tem and at the same energy but are inconsistent at the several- σ level, even larger discrepancies may be expected when comparing many types of scattering observables on different nuclei and energies during global OMP parameter inference. (It is worth mentioning that, of the data types considered for training OMPs, such experimental uncertainty underestimation appears to be most acute for differential elastic scattering data.) To be reliable, any data-driven assessment of OMP uncertainty must address this unaccounted-for dispersion of the experimental data. Moreover, if we can determine how large such unaccounted-for uncertainty must be to bring the optimized OMP and experimental data into agreement, we gain insight into the degree of mutual consistency between the OMP and the data libraries used to train the OMP.

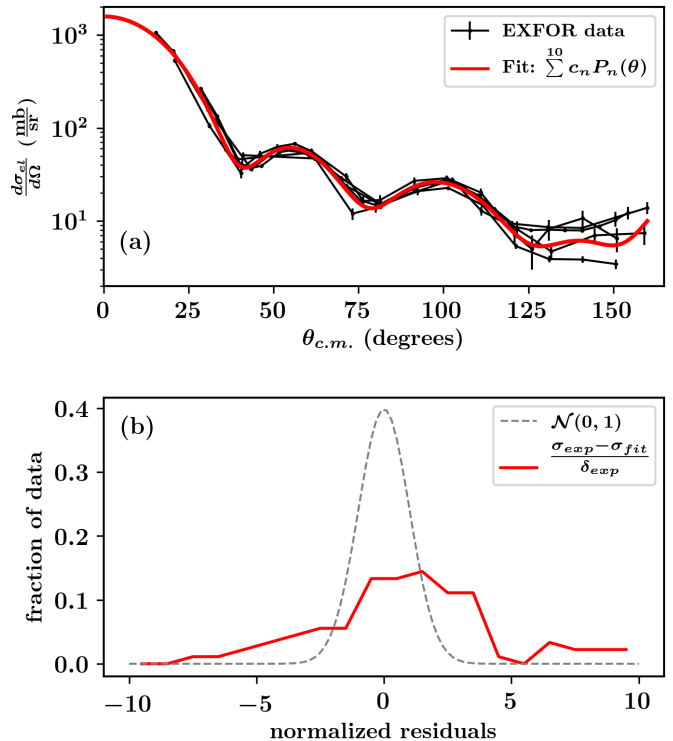


FIG. 3: Five experimental data sets for $^{40}\text{Ca}(n,n)^{40}\text{Ca}$ at 14 MeV show significant variability, despite being collected under similar kinematic conditions. In panel (a), each data set is shown as a series of black points with the reported experimental uncertainties. A weighted-least-squares fit of all points, using the sum of the first ten Legendre polynomials as a model, is shown in gray. Panel (b) shows the normalized residuals for the experimental data points as a histogram (red line). A Gaussian distribution with unit variance is shown for reference (gray dashed line).

III. IMPROVED INFERENCE FOR OMPs

In this section, we present our implementation for improved OMP parameter inference. We propose a modified likelihood function that addresses the problems of canonical OMP analysis as identified in the previous section. We then describe our implementation of the CH89 and KD OMPs, our scattering code, and the MCMC tools we used for performing parameter inference.

A. Likelihood function

For a training corpus consisting of N experimental data, denoted $(\mathbf{x}, \mathbf{y}, \delta_{\mathbf{y}})$, and an OMP with k free parameters θ , we define our likelihood function as follows:

$$L(\mathbf{y}|\mathbf{x}, \delta_{\mathbf{y}}, \theta, \delta_{\mathbf{u}}) = \frac{1}{\sqrt{(2\pi)^k |\tilde{\Sigma}|}} e^{-\frac{1}{2} \mathbf{r}^T \tilde{\Sigma}^{-1} \mathbf{r}}, \quad (10)$$

$$\mathbf{r} \equiv \mathbf{y} - M(\theta, \mathbf{x}).$$

In place of the true (unknown) data covariance matrix Σ , we have introduced a diagonal covariance matrix ansatz $\tilde{\Sigma}$:

$$\tilde{\Sigma} \equiv \frac{k}{N} \begin{bmatrix} \Delta_1 & & \\ & \ddots & \\ & & \Delta_N \end{bmatrix}; \Delta_{1,\dots,N} \in \mathbf{\Delta}. \quad (11)$$

In this prescription, the augmented variances $\mathbf{\Delta}$ combine the experimentally reported uncertainties $\delta_{\mathbf{y}}$ with an new unaccounted-for uncertainty for each datum, $\delta_{\mathbf{u}}$:

$$\mathbf{\Delta} = \{(\delta_y^2 + \delta_u^2) : \delta_y \in \delta_{\mathbf{y}}, \delta_u \in \delta_{\mathbf{u}}\}, \quad (12)$$

where each δ_u is calculated as follows:

$$\delta_u = \left\{ \frac{y + M(\boldsymbol{\theta}, x)}{2} \times \delta_t : x \in \mathbf{x}, y \in \mathbf{y}, \delta_t \in \delta_{\mathbf{T}=\hat{t}(\mathbf{y})} \right\}. \quad (13)$$

To clarify these expressions, we start with the terms in Eq. 13. As discussed in the previous section, the reported uncertainties for experimental measurements are often too small to be self-consistent, hindering robust OMP UQ assessment. As such, we need a way of increasing our uncertainty in the experimental data that is consistent with the expectation that different types of experimental data (differential elastic cross sections, neutron total cross sections) will have different degrees of uncertainty underestimation. At the same time, we want to respect the reported experimental uncertainty, as it represents the measurer’s informed judgement about uncertainty affecting the measurement, even if in aggregate, they are often underestimated. Our solution is to create a random variable δ_T , representing *unaccounted-for uncertainty*, for each type of experimental data appearing in the training corpus. For example, in the CHUQ training corpus, there are four types of experimental data: differential elastic scattering cross sections and analyzing powers, each for protons and neutrons. As such, we create four random variables, each representing some degree of unaccounted-for uncertainty for measured data of that type. At present, we do not know the value of these random variables δ_T , so we treat them as parameters to be learned alongside the OMP parameters $\boldsymbol{\theta}$.

Returning to Eq. 13, for each experimental datum in the training set, we calculate a datum-specific unaccounted-for uncertainty term δ_u , which is the product of the average of the model prediction $M(\boldsymbol{\theta}, x)$ and the experimental datum value y with the unaccounted-for uncertainty δ_T of that datum’s data type. (The term $\delta_{\mathbf{T}=\hat{t}(\mathbf{y})}$ should be read as “a N -long vector of δ_T values, each corresponding to the data type of experimental measurement y ”.) Thus for each datum of the same type, the individual unaccounted-for uncertainty δ_u is calculated using the same δ_T .

With δ_u defined, we proceed to Eq. 12. For each experimental training datum, the reported uncertainty δ_y is added in quadrature with that datum’s δ_u yielding the overall uncertainty Δ for that training datum. The vector of these augmented uncertainties, $\mathbf{\Delta}$, enters Eq. 11,

which defines the covariance matrix ansatz. The entries of $\tilde{\Sigma}$ are scaled by k/N in recognition that, by replacing the $k \times k$ -matrix Σ with an $N \times N$ covariance matrix ansatz $\tilde{\Sigma}$, a scaling factor is required to approximately preserve the matrix determinant that features in the overall normalization. This is equivalent to saying that the N training data cannot all be independent random variables, as the information they contain can span, most, the k dimensions of $\boldsymbol{\theta}$.

In sum, our likelihood function (Eq. 10) replaces the unknown covariance matrix Σ with a diagonal matrix of variance terms $\mathbf{\Delta}$, each of which has been augmented based on the unaccounted-for-uncertainty δ_T for each data type. If reasonable values can be learned for unaccounted-for uncertainties δ_T in tandem with $\boldsymbol{\theta}$, this approach will yield both a fitted OMP with good coverage of the training data and also a sense of the missing uncertainty required to bring the experimental data into agreement with the model. We remain agnostic about the source of the unaccounted-for uncertainty, be it underestimation of experimental uncertainty, model deficiencies, errors in the tabulation of experimental results, insufficient numerical precision during model calculations, or an “unknown unknown”. The practical effect of each Δ is the same as in traditional weighted-least-squares, namely, to reduce the contribution of residuals to the overall likelihood.

If we place the likelihood function in the the log-likelihood form relevant for optimization,

$$\log L(\mathbf{y}|\mathbf{x}, \delta_{\mathbf{y}}, \boldsymbol{\theta}, \delta_{\mathbf{T}}) = -\frac{1}{2} \left[\frac{\mathbf{r}^T \mathbf{r}}{|\tilde{\Sigma}|} + \log |\tilde{\Sigma}| + k \log (2\pi) \right]. \quad (14)$$

it becomes clear that minimizing the log-likelihood involves a competition between the first and second terms inside the brackets. Larger δ_T values make for larger $\mathbf{\Delta}$ and a larger covariance determinant $|\tilde{\Sigma}|$, which reduces the first term but increases the second term. At the optimum, where $\boldsymbol{\theta}$ minimizes the contribution from residuals, both terms should be equal,

$$\mathbf{r}^T \mathbf{r} = |\tilde{\Sigma}| \log |\tilde{\Sigma}|. \quad (15)$$

This implies that, at the start of training our OMP, our unaccounted-for uncertainty random variables δ_T will grow rapidly, to counterbalance the large residuals between model and data, but, as the fit improves and the residuals shrink, δ_T will grow smaller.

We note that the factor k/N in the covariance ansatz is the simplest but not the only choice to account for the unknown degree of correlation between individual data. For example, one might expect *a priori* that experimental data of each type (such as proton reaction cross section, neutron analyzing powers, etc.) will correlate strongly with each other, due to common features of the experimental design or ease of certain types of measurement, but correlate more weakly with data of other data types. Accordingly, one might want to ensure that each data type contributes equally to the overall likelihood, independent of how many data points it contains, so that

data types with fewer data points are not outvoted by data types with better experimental coverage. In that case, $\tilde{\Sigma}$ could be modified to be:

$$\tilde{\Sigma} \equiv \frac{k}{n_t} \begin{bmatrix} \frac{1}{N_1} \Delta_1 \\ \vdots \\ \frac{1}{N_1} \Delta_{N_1} \\ \frac{1}{N_2} \Delta_{N_1+1} \\ \vdots \\ \frac{1}{N_2} \Delta_{N_1+N_2} \\ \frac{1}{N_3} \Delta_{N_1+N_2+N_3} \\ \vdots \\ \frac{1}{N_T} \Delta_N \end{bmatrix} \times I_N \quad (16)$$

where n_t is the number of unique data types t , and N_t is the number of data points of type t , and I_N is the identity matrix of dimension N . With this choice for $\tilde{\Sigma}$, all data points of a given data type would be given equal influence for that type, and each data type would be given equal influence on the overall likelihood. Any additional information about the covariance structure of the experimental data, such as knowledge of the systematic error for one or more specific data sets, can be directly inserted to turn $\tilde{\Sigma}$ into a more-realistic block-diagonal matrix. We experimented with a handful of alternatives, including Eq. 16, and found that their impact on the final uncertainty-quantified OMPs was small except in situations where one training data type had far fewer data points than the other types (see Fig. 13 in Section IV C). Unless noted otherwise, all results in the following sections were generated using Eq. 10 as the likelihood function.

Finally, as discussed in toy-model scenarios two and four of Section II B, we still need a way of identifying outliers in the training data corpora. By outlier, we mean a datum that should not be used to train the model, either because the model is missing physics that the data capture (e.g., effects of deformation if the model assumes sphericity), or because the data are erroneous. In either of these cases, training the model to the datum would bias model parameters. To identify outliers, we implemented a procedure similar to that by Pérez, Amaro, and Arriola in their analysis of the NN interaction via partial wave analysis of NN scattering data [40], and first suggested by Gross and Stadler [41]. Briefly, in a standard NN scattering database they examined, they found that certain data collected in similar kinematic conditions were mutually inconsistent up to the experimentally reported uncertainties. Rather than reject all inconsistent data as outliers, they used an iterative procedure to simultaneously train a model to these data while updating the outlier status of each datum used for training. In the initial step, their model was fit to the full corpus of NN-scattering data. Any data lying $> 3\sigma$ away from the model, where σ was taken to be the reported experimental uncertainty, were flagged as outliers and not included in the following round of fitting. In the second round,

the model was fitted to the smaller set of “inlier” data, then the outlier status of each datum was assessed again, based on the second fit. The process was repeated until the model fit and the outlier status of each data point became stable, yielding a mutually-consistent database, up to the fitted model. Certain data that were initially incompatible with the others were thus recovered as the model fit improved over multiple iterations.

Our procedure was the same except in two respects. In our case, for σ we included both the variance of the model prediction from MCMC and the experimental uncertainty, summed in quadrature:

$$\sigma^2 = \{\delta_y^2 + \text{var}[M(\boldsymbol{\theta}, x)] : \delta_y \in \boldsymbol{\delta}_y, x \in \boldsymbol{x}\} \quad (17)$$

Second, because MCMC involves sampling noise, many walker steps are often required before walkers have time to react to changes in the outlier status of the experimental data. Thus, we updated the outlier status of the training data only at 100-step intervals during MCMC, rather than at every step.

B. CH89 and KD implementation

We turn now to the implementation of the OMPs we retrained according to our proposed approach. Both the CH89 and KD OMPs assume a spherical optical potential, smooth in scattering energy E_{lab} and target A , for modeling the projectile-target interaction. CH89 [19] was restricted to proton and neutron elastic scattering cross sections and analyzing powers on nuclei “in the valley of stability” with $40 \leq A \leq 209$ and for scattering energies of $10 \leq E \leq 65$ MeV (assumed to be the lab frame). The potential consists of five terms: a real central potential, an imaginary central potential, an imaginary surface potential, a real spin-orbit potential, and for protons, a Coulomb potential (see the Appendix for detailed functional forms). In all, these components employ 22 free parameters. To perform comparisons with experimental data, the authors of CH89 used a joint scattering-optimization code called MINOPT, a hybrid of the scattering code OPTICS [42] and the CERN optimization code MINUIT [43]. For the wave equation, the original treatment used the non-relativistic Schrödinger equation. Because the lowest considered scattering data energy was 10 MeV, the original treatment took the compound-nucleus contribution to be zero.

The KD global OMP [20] was fitted not only to proton and neutron elastic scattering cross sections and analyzing powers, but also to proton reaction (or “non-elastic”) and neutron total cross sections. The authors define its domain as “(near)-spherical” nuclei with $24 \leq A \leq 209$ for incident scattering energies of $0.001 \leq E \leq 200$ MeV in the lab frame. In addition to the potential component types used in CH89, KD adds an imaginary spin-orbit component. Each component was made substantially more flexible in energy- and asymmetry-dependence, bringing the total number of free parameters to 46. To perform comparisons with experimental data,

the developers used the scattering code ECIS-97, as accessed through a visual interface called ECISVIEW. For the wave equation, the authors “[employed] the relativistic Schrödinger equation throughout”, using “the true masses of the projectile and target expressed in atomic mass units”. To manage optimization in this higher-dimensional space, they developed a new approach they called “computational steering”: a user manually adjusted parameters in real time to achieve a good visual fit, which was followed by an automated simulated annealing procedure using the program SIMANN to achieve a quantitative optimum.

For our recharacterization of these OMPs, we adhered to the original potential forms and scattering assumptions as described above but with a few minor differences. First, scattering calculations for CH89 were performed according to the same relativistic-equivalent Schrödinger equation used for KD calculations rather than the non-relativistic treatment of the original. The effect was to slightly improve the fidelity of calculated cross sections at the highest scattering energies included in the CHUQ corpus (65 MeV). Second, for differential elastic scattering cross sections at scattering energies below roughly 10-15 MeV the elastic contribution from the compound nucleus becomes significant compared to the direct contribution from the OMP and must be included for comparison to experimental data. The authors of CH89 restricted their data corpus to scattering energies ≥ 10 MeV for this reason. For the KDUQ corpus, however, roughly 10% of the elastic scattering data were collected below 10 MeV. To enable comparison with these data, Koning and Delaroche used the compound cross section values generated by ECIS-97, the same code they used for direct scattering calculations. In our case, we generated compound elastic cross sections using the LLNL Hauser-Feshbach code YAHFC [44], using the canonical parameters of KD to generate the transmission coefficients needed for the calculation.

C. Scattering code and MCMC

For scattering calculations and parameter inference, we combined the MCMC utility EMCEE [45] with a new, lightweight C++ and Python library, TOMFOOL, that we developed to perform single-nucleon scattering calculations. Cross sections were generated via a calculable- R -matrix Lagrange-mesh method after [46, 47] detailed in the Appendix. The use of a Lagrange-Legendre basis instead of a radial basis accelerates calculations severalfold but at the cost of a small loss of precision, depending on the number of basis elements and chosen R -matrix channel radius. To ensure fair comparison with the original CH89 and KD analyses, we applied several measures to validate our calculation pipeline. First, wherever possible, we drew mathematical functions from the Gnu Scientific Library (GSL) [48]. Any necessary functions unavailable in GSL (such as optical potential functional forms and relativistic kinematics equations) were subjected to

a suite of unit and integration tests, including comparison against results from the well-tested scattering code FRESKOX [49, 50] and LISE++ [51, 52]. For relativistic calculations, in addition to treating scattering energies and angles relativistically, we use the wavenumber and optical-potential rescaling approximations given by Eqs. 17 and 20/21 of [53], the same formulae used for this purpose in FRESKOX and TALYS. Using FRESKOX we prepared a set of cross section benchmarks covering a range of scattering energies, angles and targets representative of the KDUQ corpus. Using an $N = 30$ Lagrange-Legendre basis, an R -matrix channel radius of 15 fm, a maximum partial wave angular momentum $l_{max} = 80$, and a convergence threshold of 10^{-6} for the magnitude of S -matrix elements, we achieved agreement with the FRESKOX benchmarks to 1% or better, both for our relativistic and non-relativistic implementations for CH89 and KD. This configuration was used for all scattering calculation results in our analysis. Finally, we performed numerous spot checks against the figures in the original CH89 and KD papers to confirm that our implementation of their OMPs generates the same cross sections to within the graphical resolution of the original publications.

For each OMP parameter, we assigned a weakly informative truncated Gaussian prior centered on the canonical parameter value (that is, centered on the parameter values from the original KD and CH89 publications). For each prior we set the variance based on our estimates about the sensitivity of scattering observables to changes in that type of parameter. For example, a change of 20% in a Woods-Saxon radius or diffuseness would result in large changes to the location of elastic scattering diffraction minima and would thus be relatively unlikely, but not impossible, given the level of consistency among the experimental data. In contrast, the energy-dependence of the depth of the imaginary spin-orbit potential is likely only very weakly sensitive to available experimental data, so a deviation by a factor of 2 or more from the canonical value in KD would not be surprising. Absolute upper and lower limits of the truncated Gaussian priors were set to prevent any single parameter from becoming non-physical, resulting in, for example, a negative radius. For the unaccounted-for uncertainty random variables $\delta_{\mathcal{T}}$, we assigned truncated Gaussian priors as

$$\delta_t \sim \mathcal{N}(\mu = 0.2, \sigma = 0.2; \delta_t > 0), \quad (18)$$

for differential elastic observables and

$$\delta_t \sim \mathcal{N}(\mu = 0.02, \sigma = 0.02; \delta_t > 0), \quad (19)$$

for integral observables σ_{rxn} and σ_{tot} . This corresponds to an expectation of 20% unaccounted-for uncertainty in differential data types and 2% unaccounted-for uncertainty in integral data types. We based these priors on the observed degree of agreement of the canonical KD and CH89 potentials against their training corpora and on the typical range experimentally reported uncertainties for these types of data. To begin MCMC, $8 \times k$

walkers were initialized according to

$$\boldsymbol{\theta}, \boldsymbol{\delta}_t \sim \mathcal{N}(\mu = \mu_{prior}, \sigma = 0.1\sigma_{prior}) \quad (20)$$

for CHUQ and

$$\boldsymbol{\theta}, \boldsymbol{\delta}_t \sim \mathcal{N}(\mu = \mu_{prior}, \sigma = 0.01\sigma_{prior}) \quad (21)$$

for KDUQ, with k the number of parameters subject to inference. For the MCMC proposal distribution, we used the EMCEE [45] default proposal distribution, the affine-invariant Goodman-Weare sampling prescription, but with a scaling parameter $a = 1.4$, reduced from the default value of $a = 2$ to improve the acceptance fraction given the high dimensionality of the parameter space. Sampling continued for roughly 10,000 samples until ensemble means no longer exhibited movement in any parameter dimension and the percentage of each data type that were flagged as outliers ceased to change (excepting $\approx 0.1\%$ fluctuations due to the Monte Carlo nature of sampling). Due to our expectation of very long autocorrelation times among walkers, we used only the terminal sample from each walker for all results shown below.

Our reassembly of the training data corpora used to train the canonical OMPs is detailed in the Supplemental Material [37]. While we were able to recompile and verify almost all of the training data as originally used, there were a handful of discrepancies between data as reported in the referenced literature, the data as listed in the canonical CH89 and KD treatments, and the data as listed in the EXFOR experimental reaction database. Details of these differences and references to the EXFOR accession number for the data set in question (or, if the data were not available through EXFOR, to the original literature) are provided in the Supplemental Material [37]. Because our approach involves outlier-rejection and unaccounted-for uncertainties that were as large or larger than experimentally reported uncertainties, the few discrepancies were unlikely to have any appreciable effect on our analysis.

IV. RESULTS

Our results are organized in three parts. First, we compare the performance of CHUQ against that of CH89 with respect to their training data. To assess predictive power, CHUQ and CH89 are compared against a Test corpus of new scattering data collected from 2003-2020 (after the publication of the original treatment). Next, we present a similar comparison for KDUQ and KD. Last, we discuss the comparative uncertainty of the potentials, including comparison of volume integrals and how alternative likelihood functions could affect our results.

A. CH89 vs CHUQ performance

Figures 4 and 5 show the performance of CHUQ and the canonical CH89 OMP with respect to several representative experimental data sets in the CHUQ training

corpus. Figures comparing CHUQ and CH89 over the entire CHUQ corpus are provided in the Supplemental Material [37]. Overall, the median predictions of CHUQ are very similar to the canonical CH89 predictions, with the largest differences being slightly lower predicted differential elastic cross sections from CHUQ compared to those from CH89 around 10-11 MeV, the lowest scattering energies considered in the CHUQ corpus. Compared to the canonical CH89 analysis, our use of a fully relativistic-equivalent Schrödinger equation in the present work and our relaxation of the fixed Coulomb radius parameters r_c and $r_c^{(0)}$ for CHUQ improves the angular dependence of proton differential elastic scattering predictions at higher energies on high- A targets, as shown in Fig. 6.

Figure 7 summarizes the overall performance of CHUQ against the full CHUQ corpus and against the Test corpus. The means, standard deviations, and skewnesses of the residual distributions shown in Fig. 7 are listed in Table II. Using the CHUQ corpus, we can directly compare the original treatment's uncertainty estimation (CH89 UQ in Fig. 2 and Table I) and that of the present work (CHUQ in Fig. 7, panel (a), and Table 7). Across the data types in the CHUQ corpus, CHUQ yields similar mean residuals: between -1.0 and 1.0, versus -1.7 to 1.1 for CH89 UQ. This suggests that both the canonical CH89 parameters and CHUQ's central parameter values do well at reproducing average trends of training data. In CHUQ, there is apparent tension between neutron differential elastic scattering cross sections, which are slightly underpredicted ($\mu_1 = -1.0$) and proton and neutron differential elastic scattering analyzing powers, which are slightly overpredicted ($\mu_1 = 1.0$ and $\mu_1 = 0.9$).

The main difference is that compared to CH89 UQ, CHUQ yields much smaller residual standard deviations: between 1.7 to 2.1 across data types, versus 4.0 to 9.6 for CH89 UQ. That the variance of the residuals is much closer to unity indicates that the larger parametric uncertainty of CHUQ more faithfully represents the spread of the experimental data in the CHUQ corpus. Further, the fact that the variance of CHUQ-corpus residuals remains larger than unity shows that the priors we assigned to the unaccounted-for uncertainties δ_T are preventing δ_T from becoming even larger, which would further reduce the constraining power of the training data.

Panel (b) of Fig. 7 illustrates performance of CHUQ against the Test corpus. The Test corpus includes many scattering data far beyond the prescribed range of validity given by the authors of CH89, including data collected at scattering energies from 1-10 MeV and from 65-295 MeV, proton σ_{rxn} and neutron σ_{tot} data, and data from targets with $A < 40$. The performance of CHUQ is moderately degraded on the Test corpus compared to the CHUQ corpus, with mean residuals ranging from -1.8 to 2.0 across data types, and residual standard deviations ranging from 1.3 to 3.1 for elastic observables. Though the CHUQ corpus used for training did not include either proton σ_{rxn} or neutron σ_{tot} data, CHUQ's average performance against the Test corpus in these data sectors is surprisingly good, with mean residuals of 0.3 for

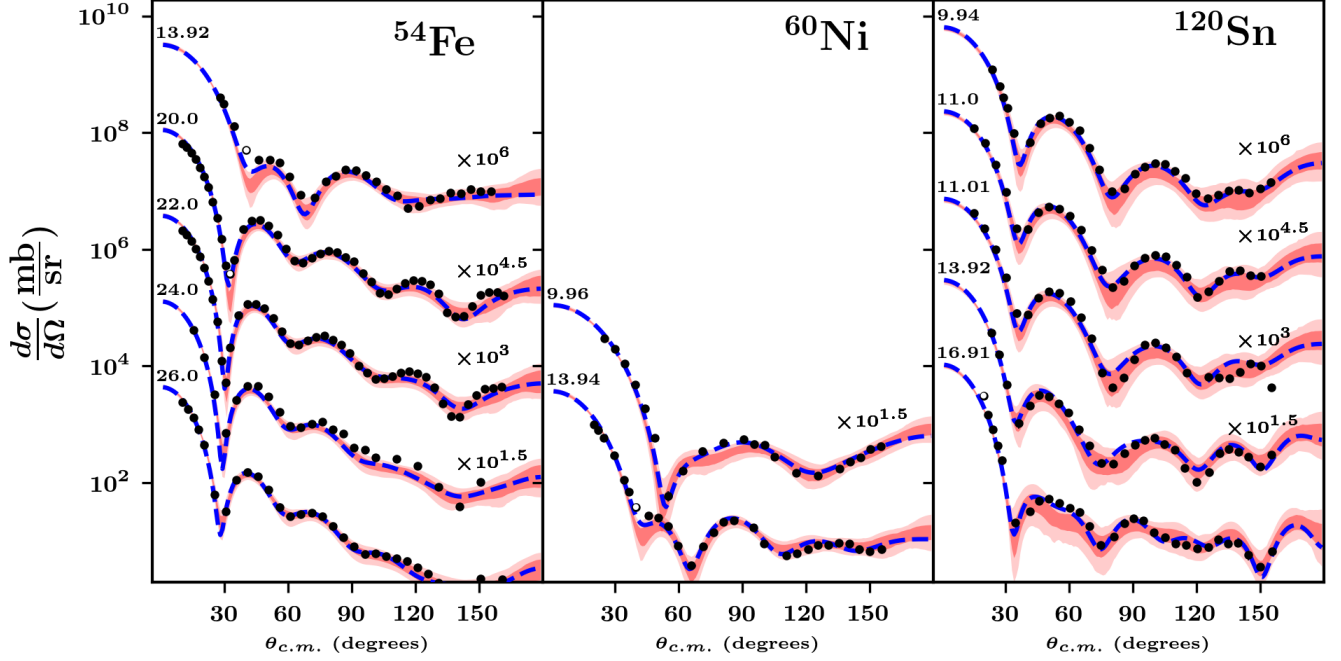


FIG. 4: Representative experimental and calculated neutron differential elastic cross sections are plotted for ^{54}Fe , ^{60}Ni and ^{120}Sn at selected energies. Experimental data are shown as points with reported experimental uncertainties. The outlier status of each point (as defined previously) is indicated by color: black points are inliers, and white points are outliers. Calculations from the canonical CH89 parameters is shown as a blue dashed line. The CHUQ 68% and 95% uncertainty intervals are shown as dark and light red bands, respectively. The data sets are labeled by scattering energy (MeV, in the lab frame) and offset vertically for legibility.

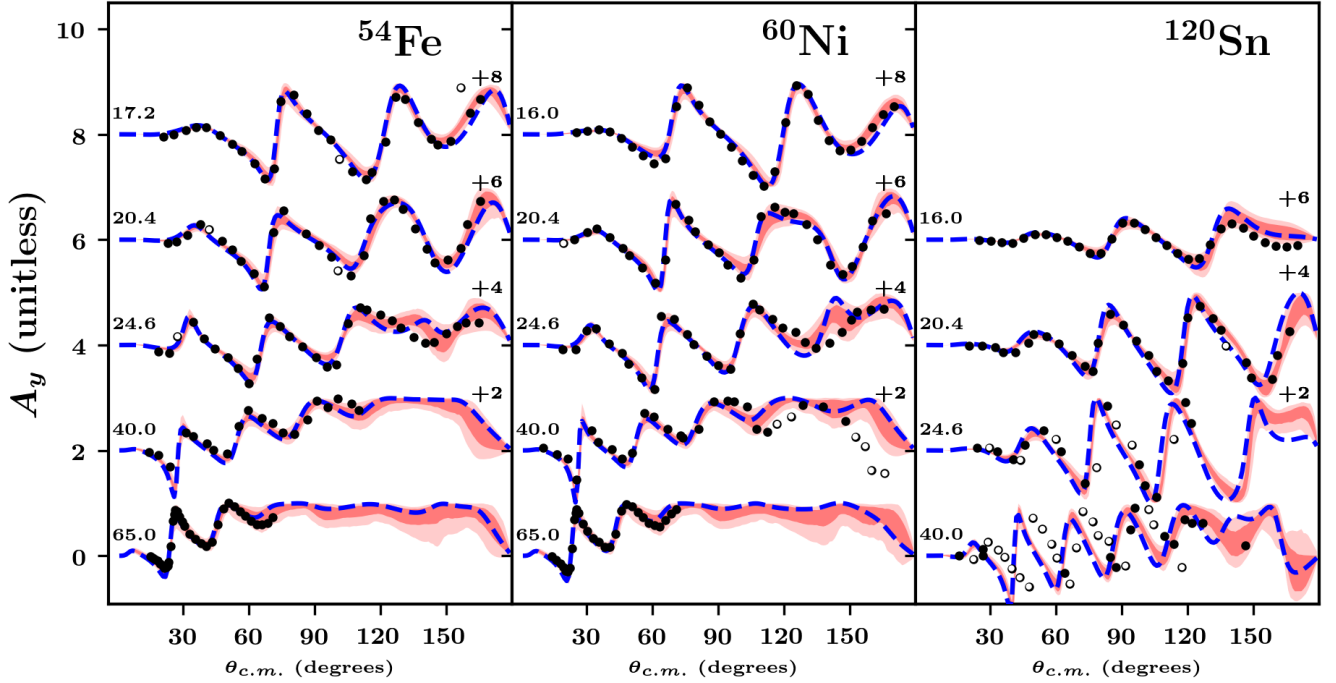


FIG. 5: Representative experimental and calculated proton analyzing powers are plotted for ^{54}Fe , ^{60}Ni and ^{120}Sn at selected energies. See caption of Fig. 4 for key.

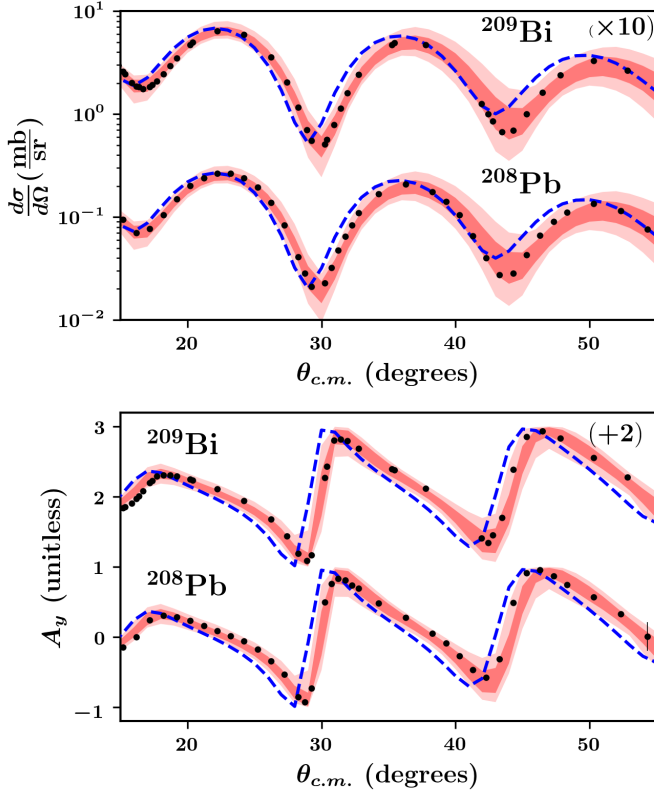


FIG. 6: CH89 and CHUQ predictions are compared against experimental proton elastic scattering observables on ^{208}Pb and ^{209}Bi at 65 MeV. See caption of Fig. 4 for key.

proton σ_{rxn} and -0.3 for neutron σ_{tot} . This indicates that despite substantial unaccounted-for uncertainty in the training data, fits that employ only elastic scattering data can still provide meaningful constraints on the imaginary terms in the potential.

B. KD vs KDUQ performance

Figures 8, 9, and 10 show the performance of KDUQ and the canonical KD Global OMP with respect to several representative experimental data sets in the KDUQ corpus used for training. Figures comparing KDUQ and KD over the entire KDUQ corpus are provided in the Supplemental Material [37]. For elastic scattering observables, the median predictions of KDUQ are very similar to the canonical KD predictions at low angles, with moderate deviations appearing at higher angles and scattering energies. Predicted neutron σ_{tot} of KDUQ and KD are nearly identical, and both achieve excellent agreement with the training data above the resolved-resonance region. (At lower energies where resonance structure is resolved, the OMP assumption of smooth, resonance-averaged behavior is no longer expected to hold). The most significant difference between KDUQ and KD is the improved reproduction of proton σ_{rxn} cross sections in KDUQ, where predictions are roughly 10% smaller for

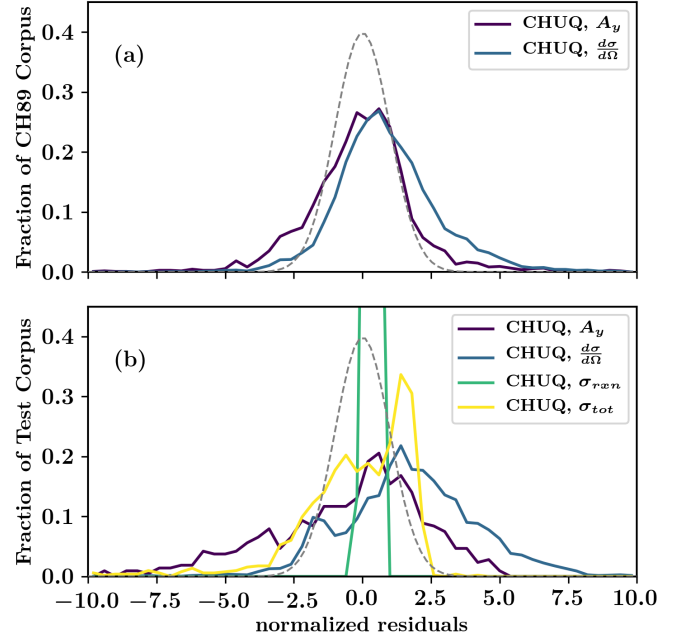


FIG. 7: Normalized residuals (r_i/δ_i) between CHUQ's predictions and the CHUQ corpus and Test corpus are histogrammed by data type. Panel (a) shows performance against the CHUQ corpus. Panel (b) shows performance against the Test corpus.

TABLE II: Mean (μ_1), standard deviation (μ_2), and skewness (μ_3) for the distributions of standardized residuals between CHUQ and experimental data, as shown in Fig. 7. Here the distributions are tabulated separately for protons and neutrons (cf. with Tables III and I).

Proton data					
	CHUQ Corpus		Test Corpus		
	$\frac{d\sigma}{d\Omega}$	A_y	$\frac{d\sigma}{d\Omega}$	A_y	σ_{rxn}
μ_1	0.0	1.0	-0.3	-1.8	0.3
μ_2	2.1	2.1	3.1	1.3	0.2
μ_3	-0.1	1.6	-0.9	-2.8	0.1
Neutron data					
	CHUQ Corpus		Test Corpus		
	$\frac{d\sigma}{d\Omega}$	A_y	$\frac{d\sigma}{d\Omega}$	A_y	σ_{tot}
μ_1	-1.0	0.9	-1.2	2.0	-0.3
μ_2	1.7	1.9	1.8	2.3	2.2
μ_3	-0.7	0.5	-0.2	0.1	-2.1

low- A targets such as ^{27}Al and ^{40}Ca compared to the predictions of KD. In addition, at scattering energies > 100 MeV across all masses, the slope of predicted proton σ_{rxn} cross sections differs between KDUQ and KD, with KD predictions exhibiting a steeper decrease with respect to energy, whereas KDUQ predictions remain roughly flat with respect to energy. Past analyses with dispersive op-

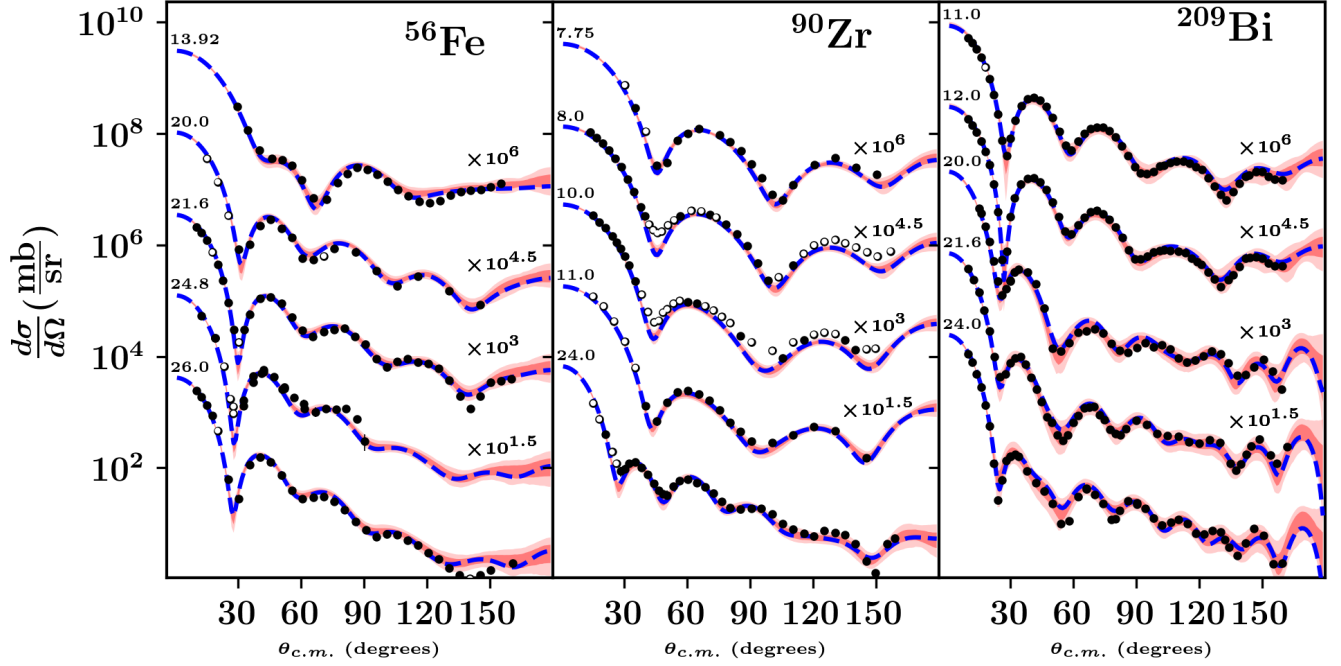


FIG. 8: Representative experimental and calculated neutron differential elastic cross sections are plotted for ^{56}Fe , ^{90}Zr and ^{209}Bi at selected energies. Experimental data are shown as points with associated uncertainties. The outlier status of each point (as defined previously) is indicated by color: black points are inliers, and white points are outliers. Cross sections calculated using the original KD formulation are shown via blue dashed line. The KDUQ 68% and 95% uncertainty intervals are shown as dark and light red bands, respectively. The data sets are labeled by scattering energy (MeV, in the lab frame) and offset vertically for legibility.

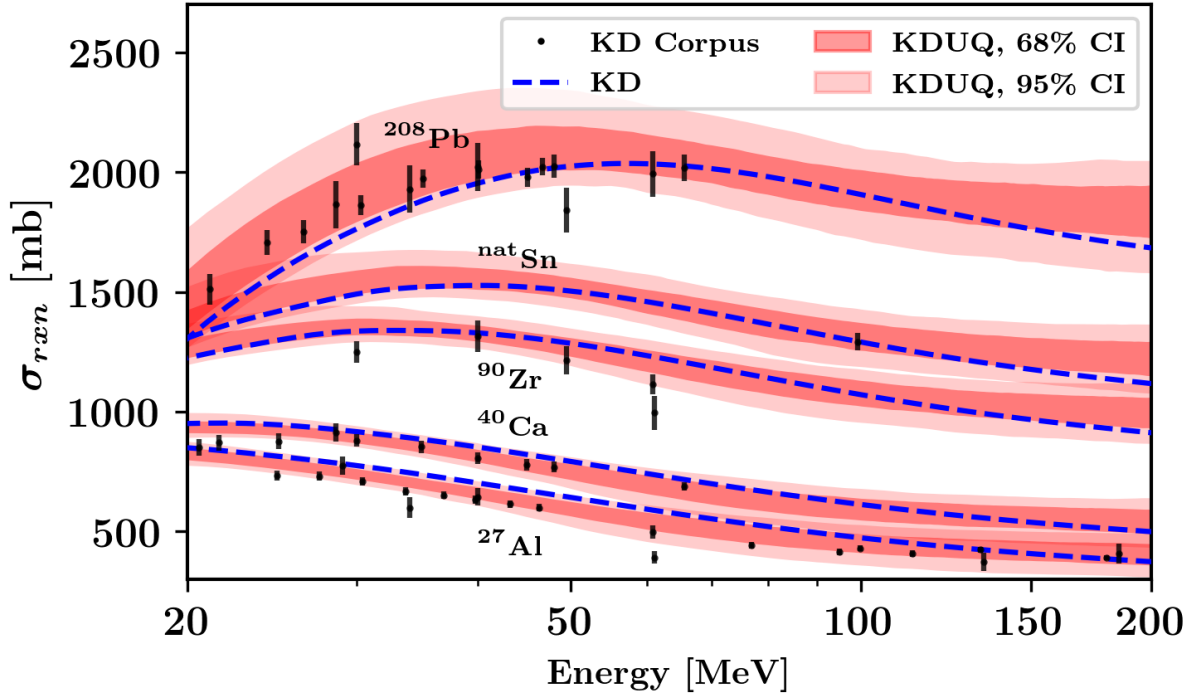


FIG. 9: Representative experimental proton reaction cross section data and KD and KDUQ calculations are plotted for selected nuclei in the KDUQ corpus. See caption of Fig. 8 for additional information on the legend.

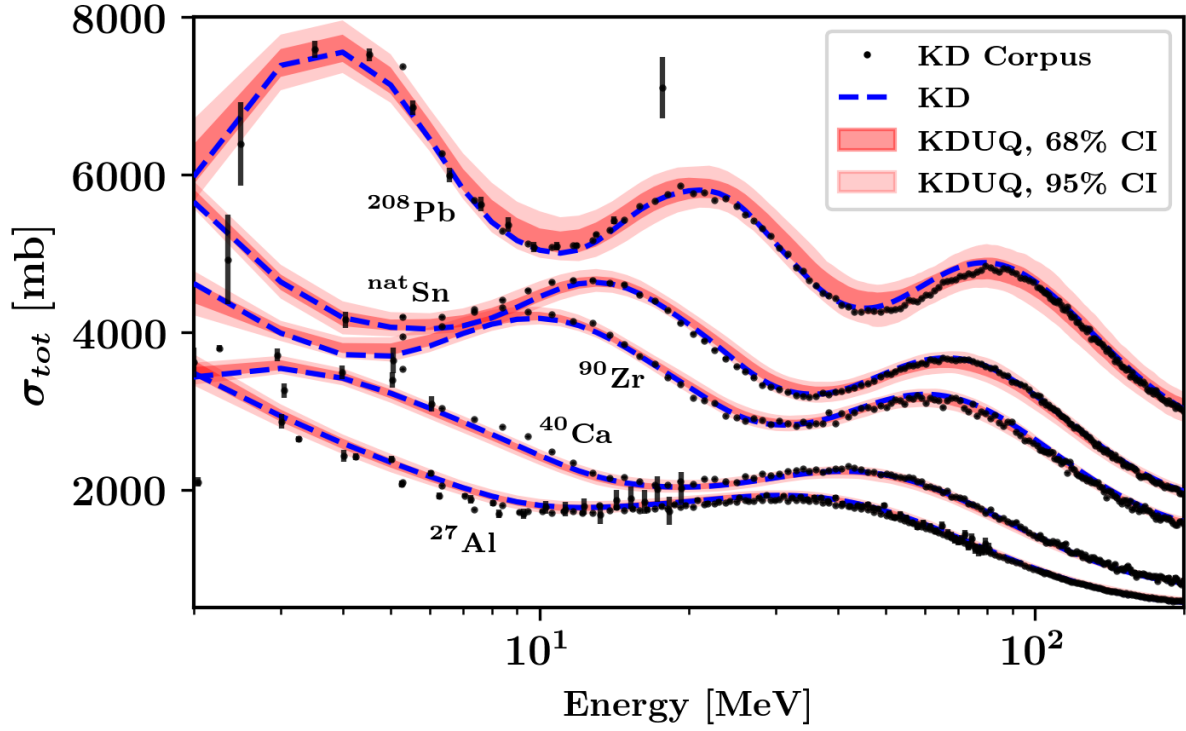


FIG. 10: Representative experimental neutron total cross section data and KD and KDUQ calculations are plotted for selected nuclei in the KDUQ corpus. See caption of Fig. 8 for additional information on the legend.

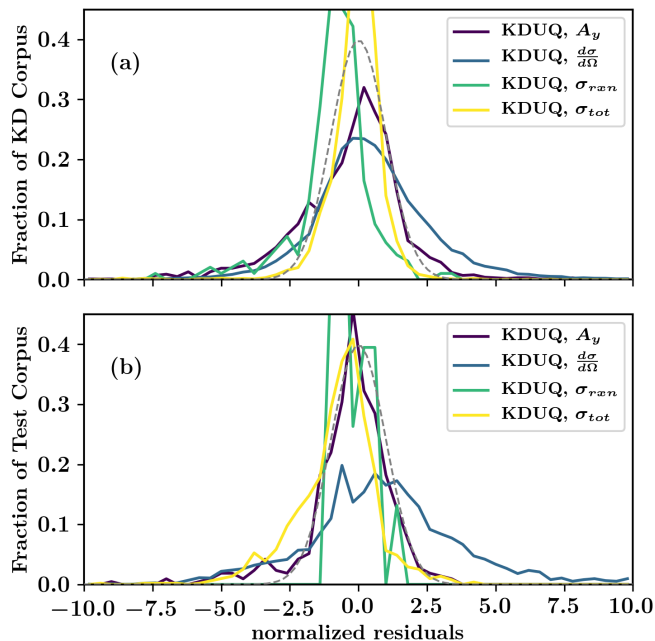


FIG. 11: Normalized residuals (r_i/δ_i) between KDUQ's predictions and the KDUQ corpus and Test corpus are histogrammed by data type. Panel (a) shows performance against the KDUQ corpus. Panel (b) shows performance against the Test corpus.

TABLE III: Mean (μ_1), standard deviation (μ_2), and skewness (μ_3) for the distributions of standardized residuals shown in Fig. 11, shown separately for protons and neutrons (cf. with Tables II and I).

Proton data						
	KDUQ Corpus			Test Corpus		
	$\frac{d\sigma}{d\Omega}$	A_y	σ_{rxn}	$\frac{d\sigma}{d\Omega}$	A_y	σ_{rxn}
μ_1	-0.1	0.5	-0.9	0.1	-0.8	-0.2
μ_2	2.2	2.1	1.5	0.9	1.8	0.7
μ_3	-0.6	1.5	-2.5	0.6	9.3	0.6

Neutron data						
	KDUQ Corpus			Test Corpus		
	$\frac{d\sigma}{d\Omega}$	A_y	σ_{tot}	$\frac{d\sigma}{d\Omega}$	A_y	σ_{tot}
μ_1	-1.1	0.5	-0.1	-1.5	1.2	-0.8
μ_2	2.1	2.3	1.2	2.0	3.3	1.5
μ_3	-0.6	0.3	-5.3	-0.8	1.1	-0.7

tical potentials have connected the energy dependence of σ_{rxn} cross sections in this region with the behavior of deeply bound, highly correlated nucleons, as probed in (e,e'p) reactions [14], and potentially correlated with neutron skins in neutron-rich nuclei [54, 55]. Such a relationship could be quantitatively assessed with a global dispersive OMP (à la [56]), but treated fully non-locally to maintain good particle number and equipped with UQ

as shown here.

Figure 11 summarizes the performance of KDUQ against both the KDUQ corpus training data and the Test corpus. The mean, standard deviation, and skewness of the distribution of residuals shown in Fig. 11 are listed in Table III for both protons and neutrons. Overall, KDUQ performance differs little between the KDUQ corpus and Test corpus, an indication that our MCMC-based approach has avoided overfitting the training data. Compared to KD, KDUQ has a lower bias with respect to proton reaction cross section data (mean normalized residual of -0.9; cf. with -2.4 for KD in Table I). Both KD and KDUQ exhibit minimal bias for neutron total cross sections (mean normalized residuals of -0.3 and -0.1, respectively). Apparently, our inclusion of unaccounted-for uncertainty terms in KDUQ is sufficient to account for almost all of the excess data variance seen for KD in Fig. 2 (neutron σ_{tot} normalized residual standard deviations of 1.2 for KDUQ, compared to 25.2 for KD). For differential elastic observables, the mean predictions from KDUQ perform similarly to those of KD against both the KDUQ corpus and the Test corpus, with the parametric uncertainty of KDUQ reducing the normalized residual standard deviations to approximately 2 for both protons and neutrons. That the normalized residual variances for differential elastic quantities are still larger than one indicates additional variance among the experimental data that the assumptions of our analysis are unable to account for. One likely source is assumption of sphericity leading to poorer agreement with differential data on more-deformed targets in the KDUQ corpus. It is well-known that, especially at low energies, only a deformation-cognizant, dispersive OMP such as those introduced by Soukhovitskii et al. [7] and Capote et al. [57] will be capable of reproducing scattering behavior. Equipping these deformed OMPs with UQ is a natural, if labor-intensive, extension. In the meantime, by examining which data are flagged as outliers in our approach, one could garner a quantitative idea of how where, and how badly, a spherical OMP fails to capture the effects of deformation on scattering.

C. Parameter comparison and discussion

In this section, we interpret the mean parameter values and uncertainties of our new UQ OMPs. Besides providing a natural way to forward-propagate OMP uncertainty via resampling, the parameter (co)variances provide information about the extrapolability of CH89- and KD-like OMPs away from their training data (e.g., away from β -stability). The optimized parameter estimates and associated uncertainties are compared in Table IV for CH89 and CHUQ and in Table V for KD and KDUQ. In addition, for a metric for the overall degree of parametric uncertainty in CH89 and CHUQ, we list the determinants of the covariance matrices for CH89 UQ and CHUQ (excluding the Coulomb radius parameters, which were fixed in the original CH89 treatment) at the bottom of Table

TABLE IV: The CH89 and CHUQ central parameter values and uncertainty intervals are listed. For CH89, the central values are the mean values reported in the original treatment, and the uncertainties are the estimated parameter standard deviations as calculated from a bootstrap analysis in the original treatment. For CHUQ, the central values are the posterior 50th percentile value and the uncertainties are the difference between the central value and the posterior 16th and 84th percentile values. The final row lists the determinant of the parameter covariance.

	CH89	CHUQ
V_0	$52.9^{+0.2}_{-0.2}$	$56.19^{+1.43}_{-1.82}$
V_t	$13.1^{+0.8}_{-0.8}$	$13.82^{+7.03}_{-5.25}$
V_e	$-0.299^{+0.004}_{-0.004}$	$-0.36^{+0.03}_{-0.02}$
r_0	$1.25^{+0.002}_{-0.002}$	$1.20^{+0.03}_{-0.03}$
$r_0^{(0)}$	$-0.225^{+0.009}_{-0.009}$	$-0.20^{+0.12}_{-0.13}$
a_0	$0.69^{+0.006}_{-0.006}$	$0.73^{+0.03}_{-0.02}$
r_c	1.24^{+0}_{-0}	$1.25^{+0.12}_{-0.12}$
$r_c^{(0)}$	0.12^{+0}_{-0}	$0.13^{+0.09}_{-0.12}$
V_{so}	$5.9^{+0.1}_{-0.1}$	$5.58^{+0.52}_{-0.58}$
r_{so}	$1.34^{+0.03}_{-0.03}$	$1.29^{+0.11}_{-0.11}$
$r_{so}^{(0)}$	$-1.2^{+0.1}_{-0.1}$	$-1.12^{+0.45}_{-0.51}$
$a_{so}^{(0)}$	$0.63^{+0.02}_{-0.02}$	$0.61^{+0.04}_{-0.04}$
W_{v0}	$7.8^{+0.3}_{-0.3}$	$9.92^{+4.63}_{-2.92}$
W_{ve0}	35.0^{+1}_{-1}	$33.15^{+25.03}_{-19.82}$
W_{vew}	16.0^{+1}_{-1}	$24.00^{+11.32}_{-9.52}$
W_{s0}	$10.0^{+0.2}_{-0.2}$	$10.59^{+3.99}_{-3.39}$
W_{st}	18.0^{+1}_{-1}	$27.09^{+12.28}_{-8.72}$
W_{se0}	36.0^{+2}_{-2}	$20.00^{+21.69}_{-20.82}$
W_{sew}	37.0^{+2}_{-2}	$36.38^{+23.75}_{-13.66}$
r_{ws}	$1.33^{+0.01}_{-0.01}$	$1.32^{+0.08}_{-0.08}$
$r_{ws}^{(0)}$	$-0.42^{+0.03}_{-0.03}$	$-0.41^{+0.36}_{-0.32}$
a_{ws}	$0.69^{+0.01}_{-0.01}$	$0.69^{+0.05}_{-0.05}$
$ \Sigma $	5.76×10^{-49}	1.08×10^{-12}

IV.

Overall, the estimated central parameter values CHUQ are similar to the original values of CH89, but in most cases, the median value from CHUQ lies well outside the estimated uncertainty of CH89 UQ. In addition, CHUQ's parametric uncertainty estimates are between two and twenty times larger than the estimates from CH89 UQ. Most notable are changes in terms affecting the potential magnitudes, including the asymmetry-dependent parameters V_t and W_{st} and the imaginary central and surface terms' A -dependent parameters W_{ve0} , W_{vew} , W_{se0} , and W_{sew} , all of which indicate far greater uncertainty with respect to target asymmetry and A than in the canonical treatment. These increased uncertainties manifest as uncertainty in the imaginary-part volume integrals as shown in Fig. 12.

The much-larger uncertainty recovered in CHUQ vs CH89 UQ is indicative of a better match of CHUQ to the breadth of the CHUQ corpus compared to the canonical CH89. However, some important details of the CHUQ corpus and Test corpus are still not captured by CHUQ,

TABLE V: The KD and KDUQ parameter values are compared and the KDUQ uncertainties listed. For KDUQ, the listed values are the posterior 50th percentile (median) value and the uncertainties are the difference between the median value and the posterior 16th and 84th percentile values.

	KD	KDUQ
$v_{1,0}$	5.93×10^1	$5.86^{+0.21}_{-0.18} \times 10^1$
$v_{1,\alpha}$	2.10×10^1	$1.34^{+0.54}_{-0.47} \times 10^1$
$v_{1,A}$	2.40×10^{-2}	$2.61^{+1.06}_{-0.99} \times 10^{-2}$
$v_{2,0}^n$	7.23×10^{-3}	$6.35^{+0.71}_{-1.05} \times 10^{-3}$
$v_{2,A}^n$	1.48×10^{-6}	$1.82^{+5.44}_{-4.74} \times 10^{-6}$
$v_{3,0}^n$	1.99×10^{-5}	$1.08^{+0.88}_{-0.93} \times 10^{-5}$
$v_{3,A}^n$	2.00×10^{-8}	$1.45^{+3.30}_{-2.77} \times 10^{-8}$
$v_{2,0}^p$	7.07×10^{-3}	$6.76^{+1.12}_{-1.32} \times 10^{-3}$
$v_{2,A}^p$	4.23×10^{-6}	$2.91^{+6.99}_{-8.20} \times 10^{-6}$
$v_{3,0}^p$	1.73×10^{-5}	$1.40^{+1.00}_{-0.94} \times 10^{-5}$
$v_{3,A}^p$	1.14×10^{-8}	$1.43^{+4.53}_{-4.47} \times 10^{-8}$
$v_{4,0}$	7.00×10^{-9}	$-4.30^{+25.60}_{-20.30} \times 10^{-9}$
$r_{V,0}$	1.30×10^0	$1.27^{+0.03}_{-0.04} \times 10^0$
$r_{V,A}$	4.05×10^{-1}	$3.61^{+1.55}_{-1.34} \times 10^{-1}$
$a_{V,0}$	6.78×10^{-1}	$6.89^{+0.24}_{-0.27} \times 10^{-1}$
$a_{V,A}$	1.49×10^{-4}	$-0.42^{+2.56}_{-2.69} \times 10^{-4}$
$r_{C,0}$	1.20×10^0	$1.19^{+0.11}_{-0.12} \times 10^0$
$r_{C,A}$	6.97×10^{-1}	$6.72^{+7.36}_{-6.60} \times 10^{-1}$
$r_{C,A2}$	1.30×10^1	$1.30^{+1.40}_{-1.26} \times 10^1$
$v_{SO1,0}$	5.92×10^0	$5.99^{+0.96}_{-0.90} \times 10^0$
$v_{SO1,A}$	3.00×10^{-3}	$1.95^{+9.63}_{-8.55} \times 10^{-3}$
$v_{SO2,0}$	4.00×10^{-3}	$4.75^{+4.07}_{-2.17} \times 10^{-3}$
$r_{SO,0}$	1.19×10^0	$1.21^{+0.06}_{-0.06} \times 10^0$
$r_{SO,A}$	6.47×10^{-1}	$7.35^{+2.58}_{-2.58} \times 10^{-1}$
$a_{SO,0}$	5.90×10^{-1}	$6.00^{+0.39}_{-0.39} \times 10^{-1}$
$w_{SO1,0}$	-3.10×10^0	$-3.79^{+2.08}_{-2.10} \times 10^0$
$w_{SO2,0}$	1.60×10^2	$2.19^{+0.84}_{-0.89} \times 10^2$
$w_{1,0}^n$	1.22×10^1	$2.09^{+0.39}_{-0.42} \times 10^1$
$w_{1,A}^n$	1.67×10^{-2}	$0.61^{+3.35}_{-2.94} \times 10^{-2}$
$w_{1,0}^p$	1.47×10^1	$1.86^{+0.56}_{-0.49} \times 10^1$
$w_{1,A}^p$	9.63×10^{-3}	$32.50^{+45.92}_{-36.72} \times 10^{-3}$
$w_{2,0}$	7.35×10^1	$10.29^{+3.45}_{-2.58} \times 10^1$
$w_{2,A}$	7.95×10^{-2}	$2.43^{+19.45}_{-16.23} \times 10^{-2}$
$d_{1,0}$	1.60×10^1	$1.67^{+0.72}_{-0.39} \times 10^1$
$d_{1,\alpha}$	1.60×10^1	$1.11^{+1.01}_{-0.79} \times 10^1$
$d_{2,0}$	1.80×10^{-2}	$2.34^{+2.56}_{-3.29} \times 10^{-2}$
$d_{2,A}$	3.80×10^{-3}	$3.73^{+30.69}_{-26.67} \times 10^{-3}$
$d_{2,A2}$	8.00×10^0	$8.57^{+7.31}_{-7.36} \times 10^0$
$d_{2,A3}$	1.56×10^2	$2.51^{+1.21}_{-2.48} \times 10^2$
$d_{3,0}$	1.15×10^1	$1.38^{+0.39}_{-0.31} \times 10^1$
$r_{D,0}$	1.34×10^0	$1.35^{+0.07}_{-0.08} \times 10^0$
$r_{D,A}$	1.58×10^{-2}	$1.75^{+1.72}_{-1.63} \times 10^{-2}$
$a_{D,0}^n$	5.45×10^{-1}	$5.43^{+0.41}_{-0.38} \times 10^{-1}$
$a_{D,A}^n$	1.66×10^{-4}	$-2.14^{+4.06}_{-4.51} \times 10^{-4}$
$a_{D,0}^p$	5.19×10^{-1}	$5.08^{+0.42}_{-0.42} \times 10^{-1}$
$a_{D,A}^p$	5.21×10^{-4}	$14.10^{+6.55}_{-6.57} \times 10^{-4}$

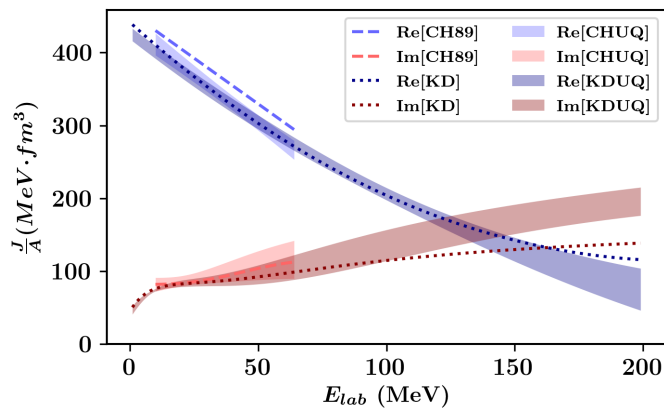


FIG. 12: Volume integrals J/A are plotted for CH89, KD, CHUQ, and KDUQ evaluated for neutron scattering on ^{90}Zr (all spin-orbit terms are excluded). The CHUQ and KDUQ bands show the 68% uncertainty interval. The ranges of CH89 and CHUQ are restricted to the nominal validity range of CH89 of 10-65 MeV.

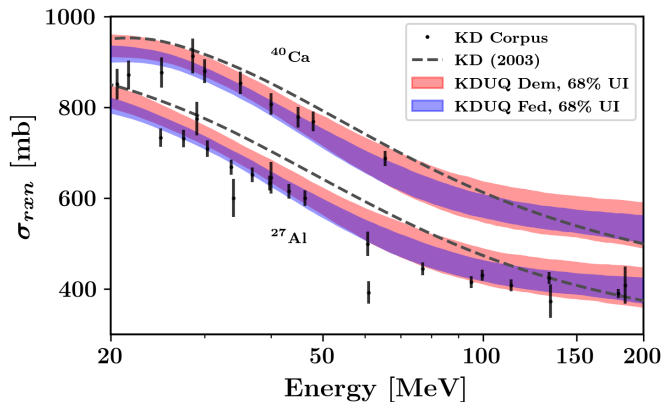


FIG. 13: A comparison of KDUQ versions trained using Eq. 11 and Eq. 16 is shown for proton σ_{rxn} on ^{40}Ca . The 68% and 95% credible intervals of appear as the dark and light bands, respectively. The experimental data of [58], [29], and [59] appear as black points with associated errors.

due to the relative simplicity of the CH89 potential form. The choice of likelihood in the canonical analysis (Eq. 8) made for good performance of the canonical CH89 parameters with respect to the experimental data, but the lack of normalization in their likelihood function resulted in an underestimation of parametric uncertainty. CHUQ performs moderately well against the Test corpus, considering that the majority of Test corpus data lie outside the nominal validity range of the CH89 potential form, but it is clear that other OMPs should be preferred at energies below 10 MeV.

We now turn to KD and KDUQ. For forty-two out of forty-six parameters, the the canonical value of KD lies within one estimated standard deviation of the KDUQ mean value; of the remaining four, three ($V_{1,\alpha}^{HF}$, $V_{2,0}^{HF,n}$,

and $V_{3,0}^{HF,n}$) are within two estimated standard deviations, and the most discrepant, $W_{1,0}^n$, lies just over two estimated standard deviations away. Notably, many sub-term parameters which are coefficients in E - and A -dependent polynomial expansions are strongly anti-correlated (see KDUQ parameter correlogram in the Supplemental Material [37]), and their estimated uncertainties are many times larger than their median values. Both these observations indicate overparameterization of E - and A -dependence in those subterms, so some of these higher-order expansion terms could likely be eliminated without impacting observables. Taken as a whole, the parameter estimates we recover are highly consistent with the canonical ones, which we take as evidence that our replication attempt, though not identical to the canonical treatment, was successful. Further, it confirms that even without the benefit of the computational advances of the last twenty years, the canonical KD analysis was remarkably close to global minimum we recover here.

In the KD/KDUQ functional form, Lane-like asymmetry-dependence appears only in two terms: the first-order energy dependence of the depth of the real volume potential as a function of asymmetry, $V_{1,\alpha}^{HF}$, and the first-order energy-dependence of the depth of the imaginary surface potential as a function of asymmetry, $D_{1,\alpha}$. For each of these parameters, KDUQ recovers significantly smaller median asymmetry-dependences than those from the canonical treatment. This implies that KD's real and imaginary surface asymmetry-dependences are weaker than previously assumed, and that the real and imaginary-surface parts of the OMP may be more reliable than previously thought when extrapolated to exotic (near-spherical) targets. At the same time, for $D_{1,\alpha}$, the uncertainties we estimate are almost as large as the median value we recover, indicating that the training data we used (coupled with our analysis assumptions) provides only a weak constraint on the behavior of the imaginary surface term away from the valley of β -stability. Considering that many downstream applications, such as r -process nucleosynthesis calculations, fission neutron spectra modeling, and planned transfer and knockout studies at NSCL and FRIB, rely on OMP-informed evaluations of low-energy inelastic cross sections on neutron-rich targets, the fact that $D_{1,\alpha}$ is poorly constrained is a pressing problem. A global, UQ-equipped phenomenological OMP analysis that incorporates isovector-sensitive observables, such as quasi-elastic charge exchange cross sections that have already yielded insight into OMP isovector dependence (e.g., [60]), is a natural next step.

Besides these terms with explicit asymmetry-dependence, the imaginary volume term, which is separately parameterized for protons and neutrons, contains information about isovector dependence of imaginary strength. For both neutrons and protons, our median-value estimates for first-order imaginary volume strength ($W_{1,0}^n$ and $W_{1,0}^p$ terms) are moderately larger than the canonical KD value, suggesting enhanced imaginary volume strength overall. Coupled with the smaller

overall imaginary surface depth $D_{1,0}$, these result in a reduction in predicted neutron/proton reaction cross sections at low energies (associated with the surface) and an increase at higher energies associated with the volume — in improved agreement with experimental trends for protons shown in Fig. 9. This trend is also visible for neutrons in Fig. 12, where above 100 MeV, the imaginary volume integral grows more rapidly for KDUQ than for KD. If verified, this additional imaginary volume strength would further quench bound-state spectroscopic factors available from dispersive optical models, as discussed in [14, 55].

Lastly, to assess the effect of our data covariance matrix ansatz on these interpretations, we compared two different versions of KDUQ: one trained using the “democratic” covariance ansatz of Eq. 11 and one trained using the “federal” covariance ansatz of Eq. 16. Figure 13 shows results from both treatments on predictions of proton σ_{rxn} above 50 MeV, where the effects of changing the covariance ansatz is largest. Overall, these different ansatzes have little effect on the median parameter values. However, in the case where one training data type has far fewer data than others, the federal ansatz leads to a moderate reduction of unaccounted-for uncertainty required to reproduce data of that type, which leads to more precise predictions for data of that type. This agrees with our expectation that the more realistic the experimental data covariance matrix ansatz is, the less unaccounted-for uncertainty is required to achieve good reproduction of the data.

V. IMPACT

In this section, we apply our UQ-equipped OMPs to two case studies: predicting neutron σ_{tot} evolution with respect to asymmetry, and propagation of OMP UQ into Hauser-Feshbach calculations of (n,γ) on ^{95}Mo and (p,γ) on ^{87}Sr .

A. Case study 1: evolution of neutron total cross sections in isotopic pairs

Cross sections for neutron-induced reactions on β -unstable targets are a key input for several nuclear data applications, e.g., r -process nucleosynthesis network calculations [61]. Because of the experimental difficulty in performing cross section measurements in this regime, cross sections estimations rely on either (semi-)microscopic OMPs [2, 5] or phenomenological potentials fitted solely to stable-target data, such as the KD global OMP, that are then extrapolated according to their assumed asymmetry-dependence. For incident neutrons at lower energies (< 10 MeV), the asymmetry-dependence of the imaginary surface term strongly affects capture cross sections [25], but the magnitude of this asymmetry-dependence remains poorly known. More broadly, such isovector components of optical potentials are connected

to other poorly constrained but important nuclear quantities, such as neutron skins in finite nuclei [14, 55, 59] and the density-dependence of the symmetry energy, L , in nuclear matter, which influences both the theoretical limit to neutron star radii and the dynamics of neutron star mergers, among other properties [62]. As such, improving our knowledge of the appropriate asymmetry-dependence of OMPs remains an important task.

To constrain asymmetry-dependent terms of phenomenological OMPs, past analyses have focused mainly on two types of experimental data: quasielastic charge exchange cross sections to the isobaric analog state (as analyzed in [60] using a KD-like potential), and ratios of neutron cross sections measured on different isotopes along an isotopic or isotonic chain (as studied by [29, 58, 59, 63, 64]). Quasielastic charge exchange is an ideal probe in that measured cross sections are sensitive specifically to isovector strength, but analysis of these data may require more sophisticated theoretical machinery (as compared to straightforward elastic and total cross section calculations) to correct for contamination from $\Delta J^\pi \neq 0^+$ channels, as demonstrated in [65]. The second type, ratios of neutron cross sections, has the advantage that by taking a cross section ratio, many systematic uncertainties (such as detector efficiency) are divided out. Further, if more than two isotopic targets are available, multiple ratios can be constructed and additional quantities, such as degree of deformation, can be extracted [63, 64]. In addition, because neutron total cross sections can be simultaneously collected from a few to a few hundred MeV [66, 67] at precisions of $\approx 1\%$, ratios of neutron total cross sections can provide information about OMP isovector features across broad regime of energies relevant for OMP construction and application. The main drawback of this type of measurement is the often-prohibitive expense of obtaining large, isotopically pure targets with precisely known areal densities. Even when isotopically pure targets are available along an isobar or isotopic chain, because they must be stable or at least long-lived to be suitable for target fabrication, they can span only a small range of asymmetries, which diminishes the isovector signal in the cross section ratio.

The importance of constraining isovector terms warrants a future, global OMP analysis including both of these data types as well as neutron strength functions (as used by [5]) to characterize isovector dependence. As a precursor to such an analysis, in Fig. 14 we consider canonical KD OMP and KDUQ predictions against neutron total cross section isotopic ratios on $^{40,48}\text{Ca}$ [58], $^{58,64}\text{Ni}$, $^{112,124}\text{Sn}$, [29], $^{182,186}\text{W}$ [59]. In all instances, the median predicted value from KDUQ closely follows the canonical KD predictions. Due to the small reported uncertainties of the experimental data shown in Fig. 14, the canonical KD predictions are discrepant with the experimental data at the several- σ level in many places, e.g., the ^{64}Ni - ^{58}Ni relative difference below 20 MeV in panel (b). As such, if one considers just the canonical KD curve, one might conclude that the KD potential form is missing some important asymmetry-dependent

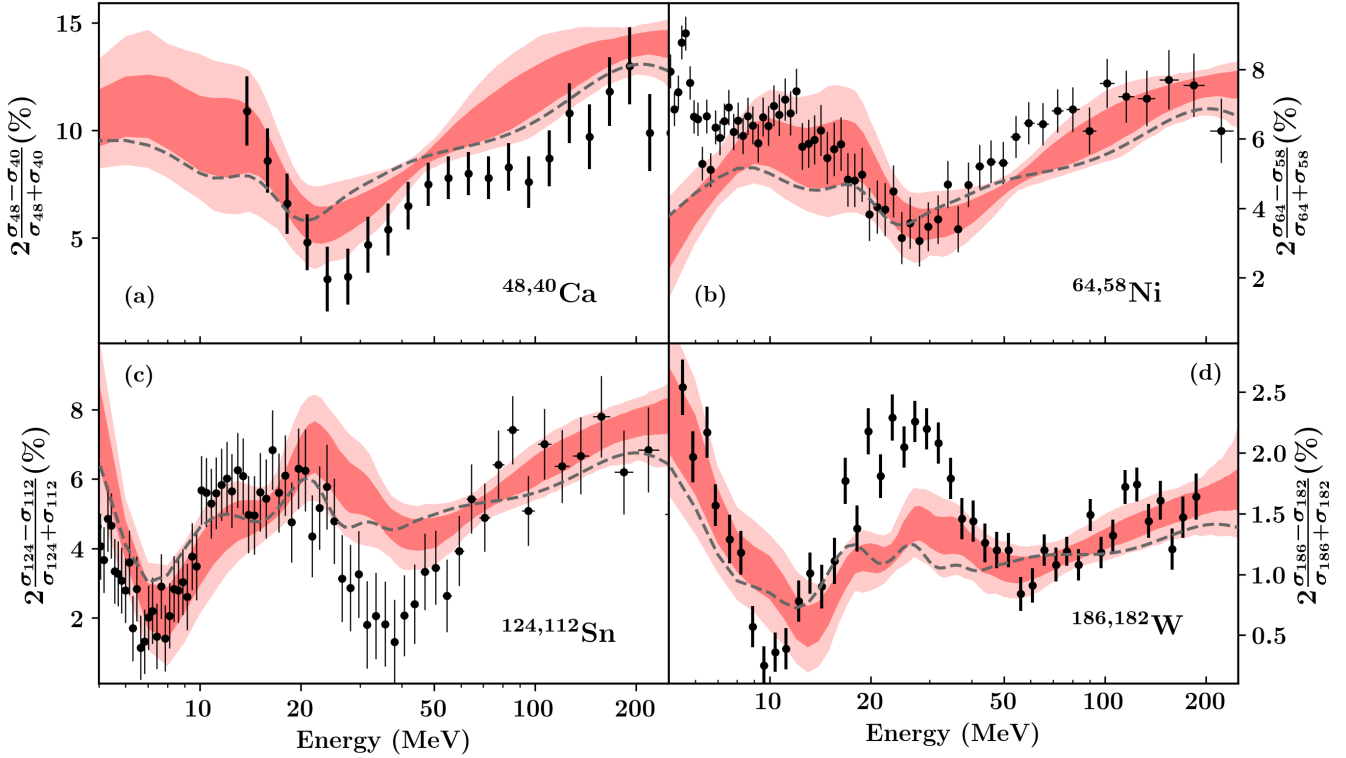


FIG. 14: Relative differences of neutron total cross sections from 5 to 250 MeV for several isotopic pairs are plotted. Calculations using the standard KD global potential are shown via the blue dashed line. The 68% and 95% credible intervals of KDUQ appear as the dark and light red bands, respectively. The experimental data of [58], [29], and [59] appear as black points with associated errors.

physics that are present in the data. However, when OMP parametric uncertainties are considered (as shown in the KDUQ curve), it is clear that most of the discrepancies between the canonical KD predictions and experimental data are not statistically meaningful. That is, once parameter uncertainties are included, the KD potential form is quite effective at predicting these cross section ratios to which it was never trained. Moreover, any discrepancies that remain after parametric uncertainty is considered (for example, the overprediction of the Sn isotopic ratios, shown in panel (c), between 30 and 50 MeV), become even more interesting: they *do* indicate residual physics that has been captured by the measurement, but not by the assumptions of our OMP. In the specific case of Sn and W isotopic ratios, the likely cause for the significant discrepancy between predictions and measurements is that the KD form, by definition, neglects the differing density profiles for neutron and protons in the Sn and W isotopes. Indeed, Dietrich et al. [59] who collected the W data found that accurately reproducing the W isotopic ratio data between 20 and 40 MeV required a Jeukenne-Lejeune-Mahaux-inspired coupled-channel OMP analysis that featured an increasing neutron skin from ^{182}W to ^{186}W . If more isotopically resolved neutron total cross section ratios were available, a similar analysis across many isotopic chains could provide neutron skin thicknesses and additional information

on L , though the potential would need to be deformation-aware and not spherical, as assumed here. The apparent (but, in light of the parametric uncertainty, insignificant) discrepancy between the canonical KD calculation and the Ni isotopic ratio data is an example of how well-calibrated UQ helps avoid mistaking noise in the experimental data for signal. At the very least, the KDUQ predictions make clear that in order for neutron total cross section ratios to constrain asymmetry-dependent OMP terms for a KD-like potential, the relative difference measurement must achieve 1% precision or better.

B. Case study 2: $^{95}\text{Mo}(n,\gamma)^{96}\text{Mo}$ and $^{87}\text{Sr}(p,\gamma)^{88}\text{Y}$ cross sections

One of the most common applications for OMPs is as an input for radiative capture calculations. While direct and pre-equilibrium capture mechanisms play an important role for light and near-dripline nuclei [70], the Hauser-Feshbach model, which assumes equilibration of the excited composite nucleus before de-excitation, is appropriate for most nucleon capture reactions. In this picture, both the probability of creating a compound nucleus in the entrance channel and the evaporation of nucleons from an excited nucleus depend on energy- and angular-momentum-dependent transmission coefficients

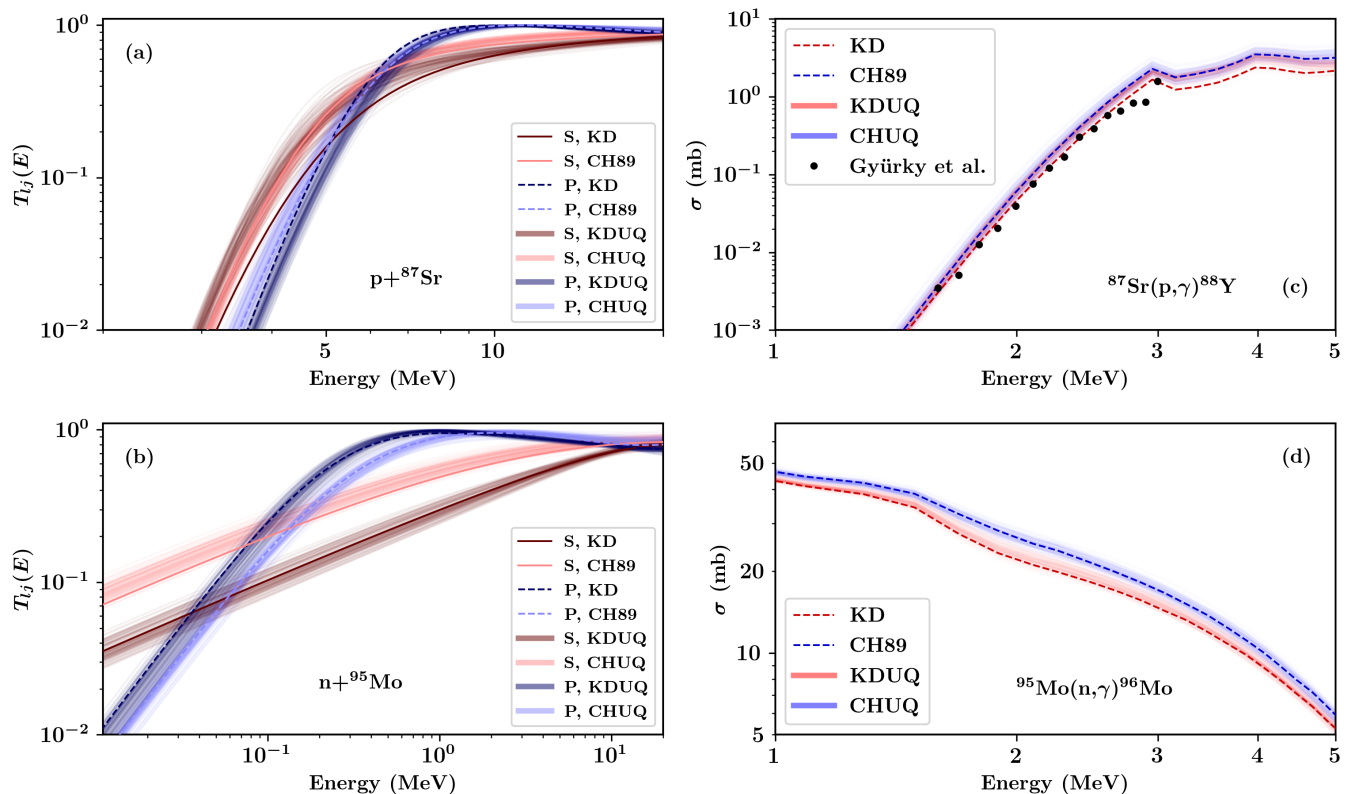


FIG. 15: Transmission coefficients and cross sections for $^{87}\text{Sr}(p,\gamma)^{88}\text{Y}$ and $^{95}\text{Mo}(n,\gamma)^{96}\text{Mo}$ are plotted. All calculations were performed using the statistical reaction code YAHFC [44] with default structure inputs. Calculations using the canonical KD OMP are shown via blue lines; calculations using CH89 are shown as red lines. Calculations using 100 samples each from the KDUQ and CHUQ posterior distributions are shown as diffuse blue and red bands, respectively. In panels (a) and (b), both S -wave ($L=0, J=\frac{1}{2}$) and P -wave ($L=1, J=\frac{3}{2}$) transmission coefficient curves are shown. Panel (c) includes experimental data from Gyürky et al. [36] (scaled upward by a factor of 2.5 to agree with the $^{88}\text{Sr}(p,\gamma)^{89}\text{Y}$ data of [68], as indicated by Vagena et al. [69]).

$T_{lj}(E)$ that are determined by an OMP. To illustrate the relative impact of OMP uncertainty on nucleon capture within the Hauser-Feshbach model, we propagated CHUQ and KDUQ uncertainties through two representative reactions: $^{95}\text{Mo}(n,\gamma)^{96}\text{Mo}$ and $^{87}\text{Sr}(p,\gamma)^{88}\text{Y}$ at incident nucleon energies up to 5 MeV. Calculations were carried out using the LLNL Hauser-Feshbach code YAHFC [44], modified to accept KD-like and CH89-like potentials with arbitrary parameters, and using YAHFC default configuration information, discrete level data, nuclear level densities (LDs), and γ -ray strength functions (γ SFs). For each reaction, we ran YAHFC once using the canonical KD and once using the canonical CH89 potential and then performed one hundred YAHFC runs each for CHUQ and KDUQ, with each run using a unique sample of the OMP parameter posterior. Results of these calculations are shown in Fig. 15. Panels (a) and (b) show transmission coefficients $T_{lj}(E)$ generated by YAHFC's invocation of FRESKOX [50] for protons incident on ^{87}Sr and for neutrons incident on ^{95}Mo . Panels (c) and (d) display the corresponding capture cross sections, where the uncertainty shown is due to the transmission coefficients of panels (a) and (b). As YAHFC

uses a Monte Carlo approach for de-exciting compound nuclei, we drew 10^6 samples at each scattering energy to ensure that YAHFC's statistical uncertainty due to Monte Carlo sampling was less than 1% for the calculated capture cross sections.

For $p+^{87}\text{Sr}$, the CH89, CHUQ, and KDUQ transmission coefficients show overall consistency across all depicted energies, whereas the KD transmission coefficients are slightly lower than the other OMPs between 3 and 10 MeV. The principle difference for KD was reduced s -wave strength and a more rapid rise in p -wave strength. Below 3 MeV the Coulomb barrier manifests as a steep reduction across the board. Above 10 MeV (the minimum energy included in the CHUQ corpus), the $T_{lj}(E)$ generated from all four OMPs are consistent within approximately 10%, an indication that the OMP uncertainty is likely a minor source of uncertainty in cross section predictions above this energy.

This reaction was one of those considered by Vagena et al. in their recent study [69] of systematic effects of the proton OMP on p -process nucleosynthesis. In their approach, using TALYS they sought to improve the Bruyère-le-Châtel version of the Jeukenne-Lejeune-Mahaux semi-

microscopic proton OMP [5] by tuning its parameters to better reproduce experimental cross sections for specific reactions. In the case of $^{87}\text{Sr}(p,\gamma)^{88}\text{Y}$, experimental data were available from 1.6 to 3 MeV as collected by Gyürky et al., shown here in panel (c) of Fig. 15. Following Vagena et al., we have scaled the data up by a factor of 2.5 from the original publication to comport with $^{88}\text{Sr}(p,\gamma)^{89}\text{Y}$ data subsequently published by [68]. In their analysis, they argued that below roughly 3 MeV, this reaction can be considered independent of the ^{88}Sr LD and γSF , so any remaining discrepancy between predictions and measured data serves as a basis for adjusting OMP parameters. In our case, while we did not perform calculations using any microscopic OMPs, all four global phenomenological OMPs we *did* consider – CH89, CHUQ, KD, and KDUQ – generate predictions within a few tens of percent of the experimental cross sections. This suggests that unless both the LD and γSF are known within a few tens of percent precision for a given reaction, constraining OMP parameters by working backwards from measured capture cross sections may not be feasible. A consistent joint treatment combining all of these sources of uncertainty is a next step in which the yet-unknown correlations between OMPs, LDs, and γSF s will be critically important. We hope to engage in a systematic study following the logic of [69] that compares microscopic OMPs with UQ-equipped phenomenological ones for astrophysically relevant reactions. At the very least, we argue that the intuition provided here on standard phenomenological OMPs can guide analysts interested in manually tuning microscopic OMP parameters to reproduce experimental scattering observables. Given our finding that the CH89 and KD uncertainty effect on capture cross sections between 1-5 MeV that we examined is on the order of tens of percent, a practitioner who encounters a larger discrepancy between their prediction and experimental data should consider other sources of uncertainty beyond the OMP parameters, such as deformation or level density uncertainty.

Finally, we consider $n+^{95}\text{Mo}$ in panels (b) and (d). Throughout the depicted energy range, CHUQ calculations are highly consistent with CH89 and KDUQ calculations with KD, but both KD-type OMPs have a much slower rise in s -wave strength with respect to energy than do the CH89-type OMPs. At energies above 100 keV the slower s -wave rise is offset by a correspondingly faster rise in p -wave strength such that resulting neutron cross section predictions, which include contributions over all incident partial waves, differ by only 20-30%, highly consistent with the degree of uncertainty seen for $p+^{87}\text{Sr}$. Importantly, for any reactions at energies below 100 keV involving primarily the s -wave transmission coefficients, CH89 and CHUQ are expected to yield a cross section two to three times higher than KD and KDUQ. In such case, the OMP uncertainty should indeed dominate the cross section, as uncertainty in the LDs and γSF s have minimum impact at lower energies (again shown in Fig. 1 and 2 of Vagena et al. [69]). Such OMP-driven uncertainty could impact both weak and strong r -process

network calculations. Comparison of the canonical KD OMP’s s - and p -wave strength functions against experimental data, as shown in Fig. 47 of Koning and Delaroche’s original analysis, suggest that at energies below 100 keV, KD-type OMPs may have a more realistic energy dependence than the CH89-type OMPs. A detailed study of OMPs uncertainty at nucleosynthetic “bottle-necks” seems a worthy follow-up.

VI. CONCLUSIONS

Phenomenological OMPs continue to play an important role in nuclear reaction calculations but lack well-calibrated UQ. Without reliable uncertainty estimates, it is difficult to assess the relative importance of OMPs on the overall uncertainty budget of applications dependent on reaction data. To address this issue, we identified two main obstacles – systematic underestimation of experimental (co)variance and a lack of outlier rejection – and developed a generic pipeline for performing UQ on phenomenological OMPs. We then applied it to the widely-used CH89 and KD global OMPs, yielding two new potential ensembles, CHUQ and KDUQ, with full covariance information between potential parameters. CHUQ and KDUQ perform favorably against their training corpora, with KDUQ showing superior performance on the Test corpus, especially for proton σ_{rxn} and neutron σ_{tot} . Accordingly, we recommend using KDUQ over CHUQ for non-elastic calculations and for calculations below 10 MeV (the stated threshold of validity for CH89). In the case of proton σ_{rxn} data, KDUQ shows improved performance compared to the canonical KD global OMP. Further, by training two versions of KDUQ with different assumed forms of data covariance, we demonstrated how small changes in underlying covariance assumptions can impact the uncertainty of predictions in data-sparse regions, as shown for high-energy proton σ_{rxn} in Fig. 13. These results caution against naïve use of a weighted-least-squares likelihood function when experimental data used for training are known to have underestimated uncertainties and non-trivial covariance structure. In the case we presented, an MCMC-based inference strategy made sense so that we could include our unaccounted-for uncertainty estimates as priors, but the need for a defensible likelihood function is just as important in any approach, Bayesian or not, involving training a model to data.

As a demonstration of their utility, we forward-propagated CHUQ and KDUQ’s parameter covariances in two case studies. In the first, we showed that KDUQ accurately predicts neutron σ_{tot} evolution with respect to asymmetry, auguring well for neutron-scattering predictions beyond the valley of β -stability, at least along closed shells in Z . Because our uncertainty-quantified model was designed to incorporate the observed variance of its training data, a discrepancy between our model and experimental data is not easily explained away as arbitrariness in the model parameters. For example, in

our examination of isotopic relative differences of neutron σ_{tot} , we saw KDUQ underpredicted the oscillations present in the experimental relative differences for Sn and W isotopes between 20 and 50 MeV (panels (c) and (d) of Fig. 14). These oscillations can be reproduced by an OMP analysis only if the different proton and neutron density distributions of the target are taken into account, as shown in [59]. Although this physics is absent from the KD or CH89 pictures, it implies that, provided one uses an uncertainty-quantified OMP and fits to relative σ_{tot} differences rather than absolute cross sections, neutron σ_{tot} data are useful for extracting neutron skin thickness information. As new reactions are pursued at modern radioactive beam facilities, this kind of comparison between uncertainty-equipped data and uncertainty-equipped models is important for calibrating our “degree of surprise” to avoid chasing down spurious signals. Systematic comparison against isovector data, including (p,n) cross sections and σ_{tot} relative differences along isotopic and isotonic chains, is a promising meeting-ground for phenomenological and microscopic OMPs.

Finally, we explored the impact of KDUQ and CHUQ on representative radiative capture calculations for ^{87}Sr and ^{95}Mo . The capture cross sections between 1-5 MeV computed using KDUQ are somewhat lower ($\approx 20-30\%$) than those using CHUQ, though with substantial uncertainty overlap. Given the systematic assessment of proton capture rate uncertainty of [69], we argue that in the few-MeV range, the fraction of overall cross section uncertainty due to the OMP is comparable to that in the γ -ray strength function and level density, and at ener-

gies below 1 MeV the OMP uncertainty may dominate. Moreover, while the partition of strength between s - and p -wave below 10 MeV are different, particularly for neutrons, the contributions from each to the overall cross sections were countervailing for ^{95}Mo . If angular momentum transfer is restricted to a single partial wave, the differences between (and uncertainty in) OMPs can be much larger, as shown for $n+^{95}\text{Mo}$ below 100 keV, and the effect on cross sections correspondingly larger. This is another region where comparison between (semi)-microscopic and phenomenological OMPs is likely to be fruitful, both for improving existing OMPs and for providing more stringent reaction rates to astrophysical nucleosynthesis calculations. To support such efforts, we enclose copies of CHUQ and KDUQ in the Supplemental Material [37].

Acknowledgements

We thank Robert Casperson and Ron Soltz for insightful discussion regarding loss function selection and Kyle Beyer for identifying corrections to the manuscript. This work was performed under the auspices of the U.S. Department of Energy by Lawrence Livermore National Laboratory under Contract DE-AC52-07NA27344. We gratefully acknowledge support from the High Energy Density Science program (HEDP) and the Defense Science and Technology internship (DSTI) for R. Rahman.

-
- [1] F. D. Becchetti and G. W. Greenlees, *Phys. Rev.* **182**, 1190 (1969), URL <https://link.aps.org/doi/10.1103/PhysRev.182.1190>.
- [2] J.-P. Jeukenne, A. Lejeune, and C. Mahaux, *Phys. Rev. C* **16**, 80 (1977), URL <https://link.aps.org/doi/10.1103/PhysRevC.16.80>.
- [3] J. Jeukenne, A. Lejeune, and C. Mahaux, *Physics Reports* **25**, 83 (1976), ISSN 0370-1573, URL <https://www.sciencedirect.com/science/article/pii/037015737690017X>.
- [4] E. Bauge, J. P. Delaroche, and M. Girod, *Phys. Rev. C* **58**, 1118 (1998), URL <https://link.aps.org/doi/10.1103/PhysRevC.58.1118>.
- [5] E. Bauge, J. P. Delaroche, and M. Girod, *Phys. Rev. C* **63**, 024607 (2001), URL <https://link.aps.org/doi/10.1103/PhysRevC.63.024607>.
- [6] G. P. A. Nobre, A. Palumbo, M. Herman, D. Brown, S. Hoblit, and F. S. Dietrich, *Phys. Rev. C* **91**, 024618 (2015), URL <https://link.aps.org/doi/10.1103/PhysRevC.91.024618>.
- [7] E. S. Soukhovitskiĭ, R. Capote, J. M. Quesada, S. Chiba, and D. S. Martyanov, *Phys. Rev. C* **94**, 064605 (2016), URL <https://link.aps.org/doi/10.1103/PhysRevC.94.064605>.
- [8] C. Mahaux and R. Sartor, *Adv. Nucl. Phys.* **20**, 1 (1991).
- [9] J. M. Quesada, R. Capote, A. Molina, M. Lozano, and J. Raynal, *Phys. Rev. C* **67**, 067601 (2003), URL <https://link.aps.org/doi/10.1103/PhysRevC.67.067601>.
- [10] B. Morillon and P. Romain, *Phys. Rev. C* **70**, 014601 (2004), URL <https://link.aps.org/doi/10.1103/PhysRevC.70.014601>.
- [11] B. Morillon and P. Romain, *Phys. Rev. C* **76**, 044601 (2007), URL <https://link.aps.org/doi/10.1103/PhysRevC.76.044601>.
- [12] J. M. Mueller, R. J. Charity, R. Shane, L. G. Sobotka, S. J. Waldecker, W. H. Dickhoff, A. S. Crowell, J. H. Esterline, B. Fallin, C. R. Howell, et al., *Phys. Rev. C* **83**, 064605 (2011), URL <https://link.aps.org/doi/10.1103/PhysRevC.83.064605>.
- [13] M. H. Mahzoon, R. J. Charity, W. H. Dickhoff, H. Dussan, and S. J. Waldecker, *Phys. Rev. Lett.* **112**, 162503 (2014), URL <https://link.aps.org/doi/10.1103/PhysRevLett.112.162503>.
- [14] M. Atkinson and W. Dickhoff, *Physics Letters B* **798**, 135027 (2019), ISSN 0370-2693, URL <https://www.sciencedirect.com/science/article/pii/S037026931930749X>.
- [15] X. Zhao, W. Sun, R. Capote, E. S. Soukhovitskiĭ, D. S. Martyanov, and J. M. Quesada, *Phys. Rev. C* **101**, 064618 (2020), URL <https://link.aps.org/doi/10.1103/PhysRevC.101.064618>.
- [16] T. R. Whitehead, Y. Lim, and J. W. Holt, *Phys. Rev. Lett.* **127**, 182502 (2021), URL <https://link.aps.org/doi/10.1103/PhysRevLett.127.182502>.

- [17] W. H. Dickhoff, R. J. Charity, and M. H. Mahzoon, *Journal of Physics G: Nuclear and Particle Physics* **44**, 033001 (2017), URL <https://doi.org/10.1088/1361-6471/44/3/033001>.
- [18] W. H. Dickhoff and R. J. Charity, *Prog. Part. Nucl. Phys.* (2018).
- [19] R. Varner, W. Thompson, T. McAbee, E. Ludwig, and T. Clegg, *Physics Reports* **201**, 57 (1991), ISSN 0370-1573, URL <https://www.sciencedirect.com/science/article/pii/0370157391900390>.
- [20] A. Koning and J. Delaroche, *Nuclear Physics A* **713**, 231 (2003), ISSN 0375-9474, URL <https://www.sciencedirect.com/science/article/pii/S0375947402013210>.
- [21] A. Koning, *Eur. Phys. J. A* **51**, 184 (2015).
- [22] H. F. Arellano and G. Blanchon, *Phys. Rev. C* **98**, 054616 (2018), URL <https://link.aps.org/doi/10.1103/PhysRevC.98.054616>.
- [23] H. Arellano and G. Blanchon, *Physics Letters B* **789**, 256 (2019), ISSN 0370-2693, URL <https://www.sciencedirect.com/science/article/pii/S0370269318309274>.
- [24] H. Arellano and G. Blanchon, *Eur. Phys. J. A* **57**, 27 (2021), URL <https://doi.org/10.1140/epja/s10050-020-00328-0>.
- [25] S. Goriely and J.-P. Delaroche, *Physics Letters B* **653**, 178 (2007), ISSN 0370-2693, URL <https://www.sciencedirect.com/science/article/pii/S0370269307009069>.
- [26] G. B. King, A. E. Lovell, L. Neufcourt, and F. M. Nunes, *Phys. Rev. Lett.* **122**, 232502 (2019), URL <https://link.aps.org/doi/10.1103/PhysRevLett.122.232502>.
- [27] A. E. Lovell, F. M. Nunes, M. Catacora-Rios, and G. B. King, *Journal of Physics G: Nuclear and Particle Physics* **48**, 014001 (2020), URL <https://doi.org/10.1088/1361-6471/abba72>.
- [28] G. Schnabel, H. Sjöstrand, J. Hansson, D. Rochman, A. Koning, and R. Capote, *Nuclear Data Sheets* **173**, 239 (2021), ISSN 0090-3752, Special Issue on Nuclear Reaction Data, URL <https://www.sciencedirect.com/science/article/pii/S009037522100017X>.
- [29] C. D. Pruitt, R. J. Charity, L. G. Sobotka, J. M. Elson, D. E. M. Hoff, K. W. Brown, M. C. Atkinson, W. H. Dickhoff, H. Y. Lee, M. Devlin, et al., *Phys. Rev. C* **102**, 034601 (2020), URL <https://link.aps.org/doi/10.1103/PhysRevC.102.034601>.
- [30] A. Koning and D. Rochman, *Nuclear Data Sheets* **113**, 2841 (2012), ISSN 0090-3752, Special Issue on Nuclear Reaction Data, URL <https://www.sciencedirect.com/science/article/pii/S0090375212000889>.
- [31] Experimental Nuclear Reaction Data (EXFOR), online. Accessed 2022-07-06., URL <https://www-nds.iaea.org/exfor/exfor.htm>.
- [32] D. Smith and N. Otuka, *Nuclear Data Sheets* **113**, 3006 (2012), ISSN 0090-3752, Special Issue on Nuclear Reaction Data, URL <https://www.sciencedirect.com/science/article/pii/S0090375212000907>.
- [33] Neudecker, Denise, Hejnal, Brooke, Tovesson, Fredrik, White, Morgan C., Smith, Donald L., Vaughan, Diane, and Capote, R., *EPJ Nuclear Sci. Technol.* **4**, 21 (2018), URL <https://doi.org/10.1051/epjn/2018026>.
- [34] D. Neudecker, D. Smith, F. Tovesson, R. Capote, M. White, N. Bowden, L. Snyder, A. Carlson, R. Casperson, V. Pronyaev, et al., *Nuclear Data Sheets* **163**, 228 (2020), ISSN 0090-3752, URL <https://www.sciencedirect.com/science/article/pii/S0090375219300729>.
- [35] S. Harissopulos, E. Vagena, P. Dimitriou, M. Axiotis, S. Galanopoulos, V. Foteinou, and A. Lagoyannis, *Phys. Rev. C* **104**, 025804 (2021), URL <https://link.aps.org/doi/10.1103/PhysRevC.104.025804>.
- [36] G. Gyürky, E. Somorjai, Z. Fülöp, S. Harissopulos, P. Demetriou, and T. Rauscher, *Phys. Rev. C* **64**, 065803 (2001), URL <https://link.aps.org/doi/10.1103/PhysRevC.64.065803>.
- [37] See Supplemental Material at [URL will be inserted by publisher] for optical potential parameter values (Supplement A), training and test data used in our analysis (Supplement B), and figures comparing potential performance against these data (Supplement C).
- [38] A. C. Aitken, *Proceedings of the Royal Society of Edinburgh* **55**, 42b (1936).
- [39] J. Brynjarsdóttir and A. O'Hagan, *Inverse Problems* **30** (2014).
- [40] R. N. Pérez, J. E. Amaro, and E. R. Arriola, *Phys. Rev. C* **88**, 064002 (2013), URL <https://link.aps.org/doi/10.1103/PhysRevC.88.064002>.
- [41] F. Gross and A. Stadler, *Phys. Rev. C* **78**, 014005 (2008), URL <https://link.aps.org/doi/10.1103/PhysRevC.78.014005>.
- [42] R. Eastgate, W. Thompson, and R. Hardekopf, *Computer Physics Communications* **5**, 69 (1973), ISSN 0010-4655, URL <https://www.sciencedirect.com/science/article/pii/0010465573900131>.
- [43] F. James and M. Roos, *Computer Physics Communications* **10**, 343 (1975), ISSN 0010-4655, URL <https://www.sciencedirect.com/science/article/pii/0010465575900399>.
- [44] W. E. Ormand, *Yahfc*, URL <https://github.com/LLNL/Yet-Another-Hauser-Feshbach-Code>.
- [45] D. Foreman-Mackey, D. W. Hogg, D. Lang, and J. Goodman, *Publications of the Astronomical Society of the Pacific* **125**, 306 (2013), URL <https://doi.org/10.1086/670067>.
- [46] P. Descouvemont and D. Baye, *Rep. Prog. Phys.* **73**, 036301 (2010), URL <https://iopscience.iop.org/article/10.1088/0034-4885/73/3/036301>.
- [47] D. Baye, *Physics Reports* **565**, 1 (2015), ISSN 0370-1573, the Lagrange-mesh method, URL <https://www.sciencedirect.com/science/article/pii/S0370157314004086>.
- [48] Galassi, M. et al., *GNU Scientific Library Reference Manual (3rd Ed.)*, URL <https://www.gnu.org/software/gsl>.
- [49] I. J. Thompson, *Computer Physics Reports* **7**, 167 (1988), ISSN 0167-7977, URL <https://www.sciencedirect.com/science/article/pii/0167797788900056>.
- [50] I. J. Thompson, *Frescox*, URL <https://github.com/LLNL/Frescox>.
- [51] O. Tarasov and D. Bazin, *Nucl. Instrum. Meth. B* **376**, 185 (2016), ISSN 0168-583X, URL <https://www.sciencedirect.com/science/article/pii/S0168583X1600224X>.
- [52] O. Tarasov, *Lise++*, URL <http://lise.nslc.msu.edu/lise.html>.
- [53] A. Ingemarsson, *Physica Scripta* **9**, 156 (1974), URL <https://doi.org/10.1088/0031-8949/9/3/004>.
- [54] M. C. Atkinson, M. H. Mahzoon, M. A. Keim, B. A. Bordelon, C. D. Pruitt, R. J. Charity, and W. H. Dick-

- hoff, Phys. Rev. C **101**, 044303 (2020), URL <https://link.aps.org/doi/10.1103/PhysRevC.101.044303>.
- [55] C. D. Pruitt, R. J. Charity, L. G. Sobotka, M. C. Atkinson, and W. H. Dickhoff, Phys. Rev. Lett. **125**, 102501 (2020), URL <https://link.aps.org/doi/10.1103/PhysRevLett.125.102501>.
- [56] B. Morillon and P. Romain, Phys. Rev. C **74**, 014601 (2006), URL <https://link.aps.org/doi/10.1103/PhysRevC.74.014601>.
- [57] R. Capote, S. Chiba, E. S. Soukhovitskii, J. M. Quesada, and E. Bauge, Journal of Nuclear Science and Technology **45**, 333 (2008).
- [58] R. Shane, R. J. Charity, J. M. Elson, L. G. Sobotka, M. Devlin, N. Fotiades, and J. M. O'Donnell, Nucl. Instrum. Meth. **614**, 468 (2010), URL <http://dx.doi.org/10.1016/j.nima.2010.01.005>.
- [59] F. S. Dietrich, J. D. Anderson, R. W. Bauer, S. M. Grimes, R. W. Finlay, W. P. Abfalterer, F. B. Bateman, R. C. Haight, G. L. Morgan, E. Bauge, et al., Phys. Rev. C **67**, 044606 (2003), URL <https://link.aps.org/doi/10.1103/PhysRevC.67.044606>.
- [60] P. Danielewicz, P. Singh, and J. Lee, Nuclear Physics A **958**, 147 (2017), ISSN 0375-9474, URL <https://www.sciencedirect.com/science/article/pii/S0375947416302895>.
- [61] R. Surman, M. Mumpower, R. Sinclair, K. L. Jones, W. R. Hix, and G. C. McLaughlin, AIP Advances **4**, 041008 (2014), <https://doi.org/10.1063/1.4867191>, URL <https://doi.org/10.1063/1.4867191>.
- [62] M. Thiel, C. Sienti, J. Piekarewicz, C. J. Horowitz, and M. Vanderhaeghen, Journal of Physics G: Nuclear and Particle Physics **46**, 093003 (2019), URL <https://doi.org/10.1088/1361-6471/ab2c6d>.
- [63] H. S. Camarda, T. W. Phillips, and R. M. White, Phys. Rev. C **29**, 2106 (1984), URL <https://link.aps.org/doi/10.1103/PhysRevC.29.2106>.
- [64] R. E. Shamu, E. M. Bernstein, J. J. Ramirez, and C. Lagrange, Phys. Rev. C **22**, 1857 (1980), URL <https://link.aps.org/doi/10.1103/PhysRevC.22.1857>.
- [65] G. C. Jon, H. Orihara, T. Niizeki, M. Oura, K. Ishii, A. Terakawa, M. Hosaka, K. Itoh, C. C. Yun, Y. Fujii, et al., Phys. Rev. C **56**, 900 (1997), URL <https://link.aps.org/doi/10.1103/PhysRevC.56.900>.
- [66] R. W. Finlay, W. P. Abfalterer, G. Fink, E. Montei, T. Adami, P. W. Lisowski, G. L. Morgan, and R. C. Haight, Phys. Rev. C **47**, 237 (1993), URL <http://dx.doi.org/10.1103/PhysRevC.47.237>.
- [67] W. P. Abfalterer, F. B. Bateman, F. S. Dietrich, R. W. Finlay, R. C. Haight, and G. L. Morgan, Phys. Rev. C **63**, 044608 (2001), URL <http://dx.doi.org/10.1103/PhysRevC.63.044608>.
- [68] S. Galanopoulos, P. Demetriou, M. Kokkoris, S. Harisopoulos, R. Kunz, M. Fey, J. W. Hammer, G. Gyürky, Z. Fülöp, E. Somorjai, et al., Phys. Rev. C **67**, 015801 (2003), URL <https://link.aps.org/doi/10.1103/PhysRevC.67.015801>.
- [69] E. Vagena, M. Axiotis, and P. Dimitriou, Phys. Rev. C **103**, 045806 (2021), URL <https://link.aps.org/doi/10.1103/PhysRevC.103.045806>.
- [70] Y. Xu, S. Goriely, A. J. Koning, and S. Hilaire, Phys. Rev. C **90**, 024604 (2014), URL <https://link.aps.org/doi/10.1103/PhysRevC.90.024604>.
- [71] R. F. Carlson, Atom. Data Nucl. Data Tables **63**, 93 (1996), URL <http://www.sciencedirect.com/science/article/pii/S0092640X96900108>.
- [72] A. Ingemarsson, J. Nyberg, P. Renberg, O. Sundberg, R. Carlson, A. Auce, R. Johansson, G. Tibell, B. Clark, L. Kurth Kerr, et al., Nuclear Physics A **653**, 341 (1999), ISSN 0375-9474, URL <https://www.sciencedirect.com/science/article/pii/S0375947499002365>.

Appendix A: Definition of optical potentials and scattering formulae

Reproduced here are the definition of the Chapel Hill '89 [19] and Koning-Delaroche [20] optical potentials, starting from the overall potential form and ending with the definitions for form subterms. Free parameters (those subject to Bayesian inference via MCMC) are denoted in this section using a **bold** typeface. For brevity we set $\hbar = c = 1$.

1. CH89 definition

The CH89 global optical potential for single-nucleon scattering consists of five terms:

$$\begin{aligned} \mathcal{U}(r, E) = & \mathcal{V}_r(r, E) - i\mathcal{W}_v(r, E) - i\mathcal{W}_s(r, E) \\ & - \mathcal{V}_{so}(r, E)(\ell \cdot \sigma) + \mathcal{V}_C(r), \end{aligned} \quad (\text{A1})$$

where

- \mathcal{V}_r is the real central potential,
- \mathcal{W}_v is the imaginary central (or ‘‘volume’’) potential,
- \mathcal{W}_s is the imaginary surface potential,
- \mathcal{V}_{so} is the real spin-orbit potential, and
- \mathcal{V}_C is the Coulomb potential (for protons only).

As with the Koning-Delaroche potential defined below, each component (except Coulomb) consists of an energy-dependent *depth* coupled with a radius-dependent *spatial form*:

$$\begin{aligned} \mathcal{V}_r(r, E) &= V_r(E) \times f(r, R_0, \mathbf{a}_0), \\ \mathcal{W}_v(r, E) &= W_v(E) \times f(r, R_w, \mathbf{a}_w), \\ \mathcal{W}_s(r, E) &= W_s(E) \times -4\mathbf{a}_w \frac{d}{dr} f(r, R_w, \mathbf{a}_w), \\ \mathcal{V}_{so}(r, E) &= 2V_{so} \times \frac{-1}{r} \frac{d}{dr} f(r, R_{so}, \mathbf{a}_{so}), \\ \mathcal{V}_C(r) &= \begin{cases} \frac{Zze^2}{2R_C} \left(3 - \frac{r^2}{R_C^2}\right), & \text{if } r < R_C \\ \frac{Zze^2}{r}, & \text{if } r \geq R_C \end{cases}. \end{aligned} \quad (\text{A2})$$

The spatial form $f(r, R, a)$ is the standard Woods-Saxon potential

$$\begin{aligned} f(r, R, a) &= \frac{1}{1 + e^{(r-R)/a}}, \\ \frac{d}{dr} f(r, R, a) &= \frac{1}{a} \left[\frac{-e^{(r-R)/a}}{(1 + e^{(r-R)/a})^2} \right]. \end{aligned} \quad (\text{A3})$$

Here R and a are radius and diffuseness parameters, respectively. The usual $R = r_0 A^{1/3}$ dependence is assumed (see Eq. A6 below for equations defining r_0 for each component), with A the nucleon number of the target. We note that for a natural-abundance target, the value

that should be taken for A is not explicitly discussed in the original formulation of CH89 or KD. A simple choice would be to use the A of the most abundant isotope, which works well for many elements but is unsatisfying in cases where the lightest or heaviest isotope is most abundant. For example, in $^{\text{nat}}\text{Ni}$ the most abundant isotope is ^{58}Ni , but the abundance-weighted nucleon number is 58.76 (a difference of 1.3% from 58). In this work, for natural targets we took for A the target’s atomic weight, which for the targets we used agrees with the abundance-weighted nucleon number to within $\approx 0.1\%$.

The CH89 energy-dependent depths are given by:

$$\begin{aligned} V_r(E) &= \mathbf{V}_0 + \mathbf{V}_e \Delta E \pm \alpha \mathbf{V}_t \\ W_v(E) &= \mathbf{W}_{v0} \left[1 + e^{\frac{\mathbf{W}_{ve0} - \Delta E}{\mathbf{W}_{vew}}} \right]^{-1} \\ W_s(E) &= (\mathbf{W}_{s0} + \alpha \mathbf{W}_{st}) \left[1 + e^{\frac{\Delta E - \mathbf{W}_{se0}}{\mathbf{W}_{sew}}} \right]^{-1} \\ V_{so}(E) &= \mathbf{V}_{so0} \end{aligned} \quad (\text{A4})$$

The nuclear asymmetry α is defined $(N - Z)/A$. As with the definition of A , for natural targets a definition for α is not given in the original potential formulation. For these targets, we took $\alpha = (A - 2Z)/Z$, consistent with our definition of A . The energy argument ΔE is the difference between the scattering energy and the volume-averaged Coulomb energy:

$$\begin{aligned} \Delta E &= E_{lab} - E_c \\ E_c &= \begin{cases} \frac{6Ze^2}{5R_c}, & \text{for protons} \\ 0, & \text{for neutrons} \end{cases}. \end{aligned} \quad (\text{A5})$$

Lastly, the radial form parameters R_i are defined as follows:

$$\begin{aligned} R_0 &= \mathbf{r}_0 A^{1/3} + \mathbf{r}_0^0, \\ R_w &= \mathbf{r}_w A^{1/3} + \mathbf{r}_w^0, \\ R_{so} &= \mathbf{r}_{so} A^{1/3} + \mathbf{r}_{so}^0, \\ R_C &= \mathbf{r}_c A^{1/3} + \mathbf{r}_c^0. \end{aligned} \quad (\text{A6})$$

In total there are 22 free potential parameters: 11 associated with the potential depths and 16 associated with the radius-dependent spatial forms. We comment that in the original CH89 treatment, only 20 parameters were free, as the authors fixed the Coulomb parameters r_c and $r_c^{(0)}$ based on a separate assessment.

2. Koning-Delaroche definition

Similar to CH89, the Koning-Delaroche optical potential for single-nucleon scattering is defined as a function of radius r and energy E :

$$\begin{aligned} \mathcal{U}(r, E) &= -\mathcal{V}_V(r, E) - i\mathcal{W}_V(r, E) - i\mathcal{W}_D(r, E) \\ &+ \mathcal{V}_{SO}(r, E)(\ell \cdot \sigma) + i\mathcal{W}_{SO}(r, E)(\ell \cdot \sigma) + \mathcal{V}_C(r), \end{aligned} \quad (\text{A7})$$

where

- \mathcal{V}_V is the real central potential,
- \mathcal{W}_V is the imaginary central potential,
- \mathcal{W}_D is the imaginary surface potential,
- \mathcal{V}_{SO} is the real spin-orbit potential,
- \mathcal{W}_{SO} is the imaginary spin-orbit potential, and
- \mathcal{V}_C is the Coulomb potential (for protons only).

In the spin-orbit components, ℓ is the orbital angular momentum quantum number for each partial wave associated with the incident projectile and σ is the spin of the incident projectile. Except Coulomb, each component consists of an energy-dependent *depth* coupled with a radius-dependent *spatial form*:

$$\begin{aligned}
\mathcal{V}_V(r, E) &= V_V(E) \times f(r, R_V, a_V), \\
\mathcal{W}_V(r, E) &= W_V(E) \times f(r, R_V, a_V), \\
\mathcal{W}_D(r, E) &= W_D(E) \times -4a_D \frac{d}{dr} f(r, R_D, a_D), \\
\mathcal{V}_{SO}(r, E) &= V_{SO}(E) \left(\frac{\hbar}{m_\pi c} \right)^2 \times \frac{1}{r} \frac{d}{dr} f(r, R_{SO}, a_{SO}), \\
\mathcal{W}_{SO}(r, E) &= W_{SO}(E) \left(\frac{\hbar}{m_\pi c} \right)^2 \times \frac{1}{r} \frac{d}{dr} f(r, R_{SO}, a_{SO}), \\
\mathcal{V}_C(r) &= \begin{cases} \frac{Zze^2}{2R_C} \left(3 - \frac{r^2}{R_C^2} \right), & \text{if } r < R_C \\ \frac{Zze^2}{r}, & \text{if } r \geq R_C \end{cases}.
\end{aligned} \tag{A8}$$

The spatial form $f(r, R, a)$ is the same Woods-Saxon defined earlier in the CH89 case (Eq. A3), with $R = r_0 A^{1/3}$. In the spin-orbit subcomponent definitions, m_π is the charged pion mass. In the Coulomb component definition, z is the projectile charge, Z is the target charge, and e^2 is the elementary charge squared (≈ 1.44 MeV·fm).

Depending on whether the user is modeling neutron or proton scattering, the energy-dependent depths appearing in Eq. A8 are given by:

$$\begin{aligned}
V_V(E) &= v_1^{n,p} [1 - v_2^{n,p} \Delta E^{n,p} \\
&\quad + v_3^{n,p} (\Delta E^{n,p})^2 - v_4^{n,p} (\Delta E^{n,p})^3] \\
&\quad + \bar{V}_c \times v_1^p [v_2^p - 2v_3^p \Delta E^p + 3v_4^p (\Delta E)^2] \\
W_V(E) &= w_1^{n,p} \frac{(\Delta E)^2}{(\Delta E)^2 + (w_2^{n,p})^2}, \\
W_D(E) &= d_1^{n,p} \frac{(\Delta E)^2}{(\Delta E)^2 + (d_3^{n,p})^2} e^{-d_2^{n,p} \Delta E}, \\
V_{SO}(E) &= v_{SO1}^{n,p} e^{-v_{SO2}^{n,p} \Delta E}, \\
W_{SO}(E) &= w_{SO1}^{n,p} \frac{(\Delta E)^2}{(\Delta E)^2 + (w_{SO2}^{n,p})^2},
\end{aligned} \tag{A9}$$

where the superscripts n, p denote different parameters used for neutrons and protons, respectively. The energy variable $\Delta E^{n,p}$ is the difference between the incident scattering energy in MeV in the lab frame and the

Fermi energy for neutrons or protons:

$$\begin{aligned}
\Delta E^{n,p} &= E - E_f^{n,p} \\
E_f^n &= -11.2814 + 0.02646A \\
E_f^p &= -8.4075 + 1.01378A.
\end{aligned} \tag{A10}$$

The potential depth parameters from Eq. A9 are defined as:

$$\begin{aligned}
v_1^{n,p} &= \mathbf{v}_{1,0} - \mathbf{v}_{1,A} A \pm \mathbf{v}_{1,\alpha} \alpha \\
v_2^{n,p} &= \mathbf{v}_{2,0} \pm \mathbf{v}_{2,A} \\
v_3^{n,p} &= \mathbf{v}_{3,0} \pm \mathbf{v}_{3,A} \\
v_4^{n,p} &= \mathbf{v}_{4,0} \\
w_1^{n,p} &= \mathbf{w}_{1,0} + \mathbf{w}_{1,A} A \\
w_2^{n,p} &= \mathbf{w}_{2,0} + \mathbf{w}_{2,A} A \\
d_1^{n,p} &= \mathbf{d}_{1,0} \pm \mathbf{d}_{1,\alpha} \alpha \\
d_2^{n,p} &= \mathbf{d}_{2,0} + \frac{\mathbf{d}_{2,A}}{1 + e^{(A - \mathbf{d}_{2,A3})/\mathbf{d}_{2,A2}}} \\
d_3^{n,p} &= \mathbf{d}_{3,0} \\
v_{SO1}^{n,p} &= \mathbf{v}_{SO1,0} + \mathbf{v}_{SO1,A} A \\
v_{SO2}^{n,p} &= \mathbf{v}_{SO2,0} \\
w_{SO1}^{n,p} &= \mathbf{w}_{SO1,0} \\
w_{SO2}^{n,p} &= \mathbf{w}_{SO2,0} \\
\bar{V}_C &= \frac{V_C Z}{r_C A^{1/3}} = \frac{6Ze^2}{5r_C A^{1/3}}.
\end{aligned} \tag{A11}$$

In these expressions, \pm should be taken as $-$ for neutrons and $+$ for protons. Our definitions for A and for the nuclear asymmetry α for natural targets are the same as used above for CH89.

Finally, the radial form parameters entering Eqs. A3 and A8 are defined

$$\begin{aligned}
r_V &= \mathbf{r}_{V,0} - \mathbf{r}_{V,A} A^{-1/3} \\
a_V &= \mathbf{a}_{V,0} - \mathbf{a}_{V,A} A \\
r_D &= \mathbf{r}_{D,0} - \mathbf{r}_{D,A} A^{-1/3} \\
a_D &= \mathbf{a}_{D,0}^{n,p} \pm \mathbf{a}_{D,A}^{n,p} A \\
r_{SO} &= \mathbf{r}_{SO,0} - \mathbf{r}_{SO,A} A^{-1/3} \\
a_{SO} &= \mathbf{a}_{SO,0} \\
r_C &= \mathbf{r}_{C,0} + \mathbf{r}_{C,A} A^{-2/3} + \mathbf{r}_{C,A2} A^{-5/3}.
\end{aligned} \tag{A12}$$

As in Eq. A11, \pm should be taken as $-$ for neutrons and $+$ for protons. In total there are 47 free potential parameters: 31 associated with the energy-dependent depths and 16 associated with the radius-dependent spatial forms.

3. Scattering formulae

In this section we list the expressions we used to calculate proton and neutron scattering observables. Our procedure follows the calculable R -matrix method outlined in Descouvemont and Baye (DB) [46], but modified (as discussed below) to be suitable for relativistic-equivalent

calculations. The scattering observables we considered can all be calculated from the scattering matrix for incident partial waves. The S matrix for the incident projectile partial wave with angular momentum l is (DB Eq. 3.24):

$$S_l = e^{2i\delta_l} = e^{2i\phi_l} \frac{1 - (L_l^* - B)R_l(E, B)}{1 - (L_l - B)R_l(E, B)}. \quad (\text{A13})$$

The S -matrix terms are equivalent to the partial wave phase shifts δ_l . Here L_l is the logarithmic derivative of the outgoing partial wave, evaluated at channel radius a . It can be expressed in terms of Coulomb functions (DB Eqs. 3.28-3.30):

$$L_l = \frac{ka}{F_l(ka)^2 + G_l(ka)^2} \times [F_l(ka)F_l'(ka) + G_l(ka)G_l'(ka) + i]. \quad (\text{A14})$$

The hard-sphere phase shift, ϕ_l , is (DB Eq. 3.26)

$$\phi_l = -\tan^{-1}(F_l(ka)/G_l(ka)). \quad (\text{A15})$$

In these expressions, F_l and G_l are the regular and irregular Coulomb functions, with F_l' and G_l' their derivatives. (In the Coulomb function notation, we have omitted the implied Sommerfeld parameter η .) $R_l(E, B)$ are the R -matrix elements, discussed below, and B is a dimensionless boundary parameter associated with the Bloch operator. As shown in Eq. 3.27 and appendix B of DB, the scattering matrix is unaffected by the choice of boundary parameter B , so B can be set to 0 to simplify the S - and R -matrix calculation algebra.

To calculate the R matrix, we used the finite-basis approximation (Eq. 3.15 in DB):

$$R_l(E, B) = \frac{1}{2\mu a} \sum_{i,j=1}^N \phi_i(a)(\mathbf{C}^{-1})_{ij}\phi_j(a). \quad (\text{A16})$$

Here E is the center-of-mass energy, μ is the reduced mass, a is the channel radius, N is the number of basis states ϕ , and \mathbf{C} is the symmetric matrix containing solutions to the inhomogenous Bloch-Schrödinger equation (Eq. 3.7 in DB),

$$\mathbf{C}_{i,j}(E, B) = \langle \phi_i | T_l + \mathcal{L}(B) + V - E | \phi_j \rangle \quad (\text{A17})$$

To solve this equation, we employed the Lagrange-mesh method of Baye [47] on an $N = 30$ Legendre-polynomial mesh. The kinetic energy T_l and Bloch $\mathcal{L}(B)$ operators on this Lagrange-Legendre mesh (which we do not reproduce here) are given by Eqs. 3.127 and 3.129 of [47]. In our case, V is the optical potential, with E the center-of-mass energy. Note, however, that the energy argument of the optical potential, e.g., E in $U(r, E)$ of Eq. A7, is the projectile energy in the *lab frame*, per the definition of CH89 and KD.

The above formulation is appropriate for the non-relativistic limit, but above a few tens of MeV, an approximate relativistic-equivalent version should be used,

requiring modification of several elements in the calculation. First, the center-of-mass energies, angles, and the relative velocity appearing in the Sommerfeld parameter should be calculated according to relativistic kinematics. Second, in the relativistic picture the reduced mass and center-of-mass wavenumber are no longer suitable to describe the relative motion between projectile and target, so approximations are required. We used the relativistic approximations of Eqs. 17 and 20 in Ingemarsson's topical study [53] that base the wavenumber on the relativistic momentum in the center-of-momentum frame and treat the center-of-momentum motion of the target as non-relativistic. These approximations modify the wavenumber and reduced mass appearing throughout this section as:

$$k \rightarrow \frac{m_1[E(E + 2m_2)]^{1/2}}{[(m_1 + m_2)^2 + 2m_1E]^{1/2}} \quad (\text{A18})$$

$$\mu \rightarrow k^2 \frac{E'}{E'^2 - m_2^2}.$$

Here, m_1 is the target rest mass, m_2 is the projectile rest mass, E is the incident projectile energy in the laboratory frame, and E' is the sum of center of mass energies of the target and projectile, plus the rest mass of the projectile. These approximations for k and μ can be inserted in the preceding equations to yield the relativistic-approximate forms that we actually used to perform calculations.

To generate scattering observables for spin-1/2 particles, two S -matrix terms, corresponding to $j = l \pm 1/2$, must be calculated for each partial wave $l > 0$. From these terms the non-spinflip amplitude $A(\theta)$ and spinflip amplitude $B(\theta)$ can be calculated for scattering angle θ :

$$A(\theta) = \frac{i}{2k} \sum_{l=0}^{\infty} e^{2i\sigma_l} (2l + 1 - (l + 1)S_l^+ - lS_l^-) P_l(\cos \theta) - \frac{\eta}{2k \sin^2 \frac{1}{2}\theta} e^{2i(\sigma_0 - \eta \log \sin \frac{1}{2}\theta)} \quad (\text{A19})$$

$$B(\theta) = \frac{i}{2k} \sum_{l=0}^{\infty} e^{2i\sigma_l} (S_l^- - S_l^+) P_l^1(\cos \theta). \quad (\text{A20})$$

Here, S_l^+ is the S -matrix element for $j = l + \frac{1}{2}$ and S_l^- is the S -matrix element for $j = l - \frac{1}{2}$ (setting $S_0^- \equiv 0$). P_l is the Legendre polynomial of degree l , P_l^1 is the associated Legendre polynomial of degree l and order m , and σ_l is the Coulomb phase shift:

$$\sigma_l = \arg \Gamma(l + 1 + i\eta), \quad (\text{A21})$$

Γ being the gamma function. Equations A19 and A20 combine Eqs. 8 and 9 of Ingemarsson, which are for spin-1/2 neutral particles, with the spinless, charged particle scattering amplitudes of DB Eq. 2.23. Specifically, the final term of Eq. A19 that involves η is the Coulomb scattering amplitude (DB Eq. 2.13).

Finally, from the scattering amplitudes, the differential elastic cross section is simply

$$\frac{d\sigma(\theta)}{d\Omega} = |A(\theta)|^2 + |B(\theta)|^2, \quad (\text{A22})$$

and the analyzing power is

$$A_y = \frac{A^*(\theta)B(\theta) + A(\theta)B^*(\theta)}{\frac{d\sigma(\theta)}{d\Omega}}, \quad (\text{A23})$$

per Eqs. 10 and 11 of Ingemarsson. The reaction (non-elastic) and total cross sections can be computed directly from the S matrix:

$$\sigma_{rxn} = \frac{\pi}{k^2} \sum_{l=0}^{\infty} (l+1)(1 - |S_l^+|^2) + l(1 - |S_l^-|^2) \quad (\text{A24})$$

$$\sigma_{tot} = \frac{2\pi}{k^2} \sum_{l=0}^{\infty} (l+1)(1 - \text{Re}[S_l^+]) + l(1 - \text{Re}[S_l^-]). \quad (\text{A25})$$